Speleothem evidence for late Miocene extreme Arctic amplification - an analogue for near future anthropogenic climate change?

Stuart Umbo[1], Franziska Lechleitner[2], Thomas Opel[3], Sevasti Modestou[1], Tobias Braun[4,5], Anton Vaks[6], Gideon Henderson[7], Pete Scott[8], Alexander Osintzev[9], Alexandr Kononov[10,11], Irina Adrian[12], Yuri Dublyansky[13], Alena Giesche[14, 15], Sebastian F.M. Breitenbach[1]

[1]Department of Geography and Environmental Sciences, Northumbria University, Newcastle-upon-Tyne, NE1 8ST, United Kingdom
[2]Department of Chemistry, Biochemistry and Pharmaceutical Sciences & Oeschger Centre for Climate Change Research, Bern, 2012, Switzerland
[3]Alfred Wegener Institute Helmholtz Centre for Polar and Marine Research, Telegrafenberg A45, Potsdam, 14473, Germany
[4]Remote Sensing Centre for Earth System Research, Leipzig University, 04103, Leipzig, Germany
[5]Potsdam Institute for Climate Impact Research (PIK), Member of the Leibniz Association, 14473, Potsdam, Germany
[6]Geochemistry and Environmental Geology Division, Geological Survey of Israel, Jerusalem, 9692100, Israel
[7]Department of Earth Sciences, Oxford University, Oxford, OX1 3AN United Kingdom
[8]Oceans Institute, University of Western Australia, Perth, 6009, Australia
[9]Speleoclub Arabika, Irkutsk, 664058, Russian Federation
[10]Irkutsk Nation al Research Technical University, Irkutsk, 664074, Russia
[11]Institute of the Earth's Crust, Russian Academy of Sciences, Siberian Branch, Irkutsk, 664033, Russia
[12]Lena Delta Wildlife Reserve, Tiksi, Sakha Republic, 678400 Russia
[13]Institute of Geology, University of Innsbruck, Innrain 52, 6020, Innsbruck, Austria
[14]U.S. Geological Survey, Alaska Science Center, Anchorage, Alaska 99508, USA
[15]Department of Earth Sciences, Cambridge University, Cambridge CB2 3EQ, United Kingdom

Correspondence to: Stuart Umbo (stuart.umbo@northumbria.ac.uk)

Abstract. The Miocene provides an excellent climatic analogue for near future runaway anthropogenic warming, with atmospheric CO_2 concentrations and global average temperatures similar to those projected for the coming century under extreme emissions scenarios. However, the magnitude of Miocene Arctic warming remains unclear due to the scarcity of reliable proxy data. Here we use stable oxygen isotope and trace element analyses, alongside clumped isotope and fluid inclusion palaeothermometry of speleothems to reconstruct palaeo-environmental conditions near the Siberian Arctic coast during the late Tortonian (8.68 ± 0.09 Ma). Stable oxygen isotope records suggest warmer than present temperatures. This is supported by temperature estimates based on clumped isotopes and fluid inclusions giving mean annual air temperatures between +6.6 and +11.1°C, compared with -12.3°C today. Trace elements records reveal a highly seasonal hydrological environment.

Our estimate of >18°C of Arctic warming supports the wider consensus of a warmer-than-present Miocene and provides a rare palaeo-analogue for future Arctic amplification under high emissions scenarios. The reconstructed increase in mean surface temperature far exceeds those projected in fully coupled global climate models, even under extreme emissions scenarios. Given that climate models have consistently underestimated the extent of recent Arctic amplification, our proxy data suggest Arctic warming may exceed current projections. If Arctic warming by 2100 matches our late Miocene estimates, it would have large-scale impacts on global climate, including extensive thawing of Siberian permafrost – a vast fossil carbon store.

1 Introduction

The Arctic and sub-Arctic regions have warmed nearly four times faster than the global average since 1979 (Rantanen et al., 2022), and this disproportionate warming is expected to continue over the coming decades (Ma et al., 2022). Climate models have consistently underestimated the magnitude of this so-called Arctic amplification (Chylek et al., 2022; Rantanen et al., 2022) and show considerable discrepancies in its predicted magnitude (Smith et al., 2020; Taylor et al., 2022). Uncertainty in Arctic temperature projections are greater than for any other region on the planet (Taylor et al., 2022).

The Arctic is home to most of the global permafrost, a crucial climate tipping element . The Earth's largest terrestrial carbon pool , thawing permafrost will play a major role in future climate trajectories. Permafrost degradation is occurring much faster, and earlier, than expected . Increasing air temperatures lead to higher permafrost temperatures: a global network of borehole measurements over the period 2007 to 2016 show warming of 0.39 ± 0.15°C in pan-Arctic continuous permafrost . Satellite data show large increases in thermokarst thaw slump rate and prevalence in Canada and east Siberia , alongside extensive methane emissions from thawing hydrate deposits in northern Siberia . Yet, the regional impacts and carbon cycle feedbacks of thawing permafrost are highly uncertain and remain a key unknown in climate models .

Temperature has long been considered the main driver of permafrost stability, but recent studies have demonstrated the importance of seasonal precipitation characteristics, with increased rainfall amount and reduced snowfall duration driving permafrost degradation . The poorly constrained regional precipitation response to Arctic amplification , alongside limited understanding of localised feedbacks and natural variability hinder estimations of future permafrost thaw. Best estimates project the extent of global thaw between 2 and 66 % by 2100, even with concerted action to decarbonise This wide range arises in part from the fact that current global climate models largely neglect feedbacks from permafrost thaw the 2015 Paris of great importance for improving projections of permafrost thaw. Detailed paleoclimate records from Arctic speleothems (carbonate cave deposits) present an excellent opportunity to verify climate models and improve future projections. This is because they can concurrently resolve the variables of temperature, precipitation, and the presence or absence of (continuous) permafrost. Since speleothem deposition requires liquid dripwater and permafrost is largely impermeable, periods of speleothem formation indicate the absence of continuous permafrost in regions of modern-day permafrost stability

Improving Arctic climatic projections is imperative for informing local adaptation efforts. Warming is driving permafrost thaw and ice retreat, impacting ecosystems, infrastructure and access to food; whilst weather-related changes are increasing natural hazards (Ford et al., 2015). Localised warming could have global impacts. The Arctic is home to most of the planet's permafrost, a crucial possible climate tipping element (McKay et al., 2022; Nitzbon et al., 2024). Permafrost is Tthe Earth's largest terrestrial carbon pool (Strauss et al., 2024), thawing and its future thawpermafrost will play a major role in potential climate trajectories. Furthermore, modelling studies suggest Greenland ice sheet mass loss, driven by Arctic warming, will be a major contributor to 21st century sea level rise, with(Hofer et al., 2020) the potential to significantly weaken the Atlantic Meridional Overturning Circulation (Hofer et al., 2020).

Detailed palaeoclimate records present an excellent opportunity to verify climate models and improve future projections. Whilst past warm intervals represent imperfect analogues for near future climate because of differences in climate forcing, these periods can provide important examples of planetary response to atmospheric warming. Recently, Steinthorsdottir and colleagues (2021b) proposed the Miocene (23.03 – 5.33 Ma) as a suitable palaeo-analogue for future anthropogenic climate change. The distribution of continental landmasses was similar to the present day (Steinthorsdottir et al., 2021b) and atmospheric pCO$_2$ concentrations close to modern levels. Reconstructions generally agree on atmospheric pCO$_2$ values between 400 and 600 ppm throughout the Miocene (Steinthorsdottir et al., 2021a). Whilst some estimates suggest this may have reached as high as 800 – 1000 ppm during the Miocene Climatic Optimum (MCO) (Rae et al., 2021), most studies suggest it was considerably lower, likely between 430 and 630 ppm (Sosdian et al., 2018; Super et al., 2018). Subsequent cooling of ca. 6℃ was coincident with a ca. 125 ppm decline in atmospheric CO$_2$ (Super et al., 2018). By the late Miocene (ca. 7 - 5.4 Ma), multiple reconstructions converge on atmospheric carbon dioxide concentrations between 300 – 500 ppm (Rae et al., 2021; Sosdian et al., 2018; Super et al., 2018), close to modern day levels (ca.420 ppm), with the upper estimate similar to those projected for the coming decades at current emission rates (Masson-Delmotte et al., 2021).

(Steinthorsdottir et al., 2021b)Burls et al. (2021) synthesised available proxy temperature reconstructions to deduce a global mean surface temperature of 21.21 ± 0.56ºC for the early Miocene. Temperatures declined rapidly following the MCO, particularly in the high latitudes, where cooling up to 8ºC is observed in marine records (Herbert et al., 2016). By the late Miocene, global mean sea surface temperature (SST) was ca. 6°C higher than present day (Herbert et al., 2016), and mean terrestrial surface temperature was ca. 4.5°C above the pre-industrial (Pound et al., 2011). Proxy reconstructions suggest a much-reduced latitudinal temperature gradient which saw Arctic mean annual temperature (MAT) 11 – 19°C warmer than present during the middle Miocene (Steinthorsdottir et al., 2021b and references therein), declining to between 5 and 6°C above pre-industrial by the late Miocene (Pound et al., 2012). Whilst this period saw the establishment of a stable Antarctic ice sheet (Miller et al., 2020), biomarker evidence suggests that ice free summers in the Arctic persisted (Stein et al., 2016).

Modelling reconstructions, driven by inferred Miocene atmospheric CO_2 concentrations, have consistently failed to reconstruct the high temperatures, and reduced latitudinal temperature gradient, seen in the Miocene proxy records (Goldner et al., 2014). It is unclear whether this discrepancy arises due to missing climatic feedbacks within climate models or consistent under/over estimation of atmospheric CO_2 concentrations and temperatures in proxy reconstructions, but resolving it is of importance for estimation of future warming. Here we present a multi-proxy analysis of four speleothems (cave carbonate deposits) from the Siberian Arctic to infer environmental conditions during the Tortonian (late Miocene). We use isotope measurements of speleothem fluid inclusions and clumped isotope analyses to estimate multi-annual mean surface air palaeotemperatures, and stable oxygen isotope and trace element data to reconstruct palaeo-hydrology and seasonality, providing a new, high precision dataset to understand Miocene climate sensitivity.

Arctic warming has consistently exceeded the Northern Hemisphere mean by a factor of 3 – 4 during Quaternary interglacials . Recently, Steinthorsdottir and colleagues (2021) proposed the Miocene (23.03 – 5.33 Ma) as a suitable palaeo-analogue for anthropogenic climate change. Late Miocene (ca. 7 – 5.4 Ma) atmospheric carbon dioxide concentrations are estimated between 400 – 600 ppm , i.e., similar to modern levels and those projected for the coming decades at current emission rates . The distribution of continental landmasses was similar to the modern day , and temperatures were considerably warmer. Global mean sea surface temperature (SST) was ca. 6°C higher than present day , and mean terrestrial surface temperature was ca. 4.5°C above the pre-industrial level .

Here we present a multi-proxy analysis of four speleothems from the Siberian Arctic to infer environmental conditions during the Tortonian (late Miocene). We use isotope measurements of speleothem fluid inclusions and clumped isotope analyses to estimate palaeotemperatures during periods of permafrost absence, and stable oxygen isotope and trace element data to

reconstruct palaeo-hydrology and seasonality. We utilise these high latitude temperature reconstructions to provide an estimate of future permafrost thaw assuming similar levels of Arctic warming in the near future.

2 Study site and sample material

2.1 Study site

135 Samples were collected from the Taba Bastaakh cliffs (N72.27°, E126.94°), which rise ca. 140 m above the eastern riverbank near the entrance of the Lena River delta, ca. 100 km northwest of Tiksi, Sakha Republic, Russian Federation (Fig. 1). The cliffs are composed of Carboniferous-aged carbonates (Mikhaltsov et al., 2018). Lower strata (up to ca. 50 m above current river level) comprises fine quartzitic sandstone, siltstone, sandy dolomite, and dolomitic limestone with sparse fossil coral and ostracod and foraminifera assemblages broadly linked to the Tournaisian (358.9–346.7 Ma) (Izokh and Yazikov, 2017). Above,

140 ca. 50 m from the riverbank, bioclastic carbonate, calcareous siliciclastics and carbonates form a subsiding platform. Continuous permafrost, 400–600 m thick, is found in this region, with an active-layer thaw depth between 0.6 and 0.4 m (Boike et al., 2019). All caves encountered during the expedition contained significant ice deposits, rendering modern speleothem formation impossible. Modern tundra vegetation is sparse, consisting mostly of flowers, grasses, mosses, and lichens, with a small number of bushes (mainly polar willow). Trees are not found above the caves today.

145
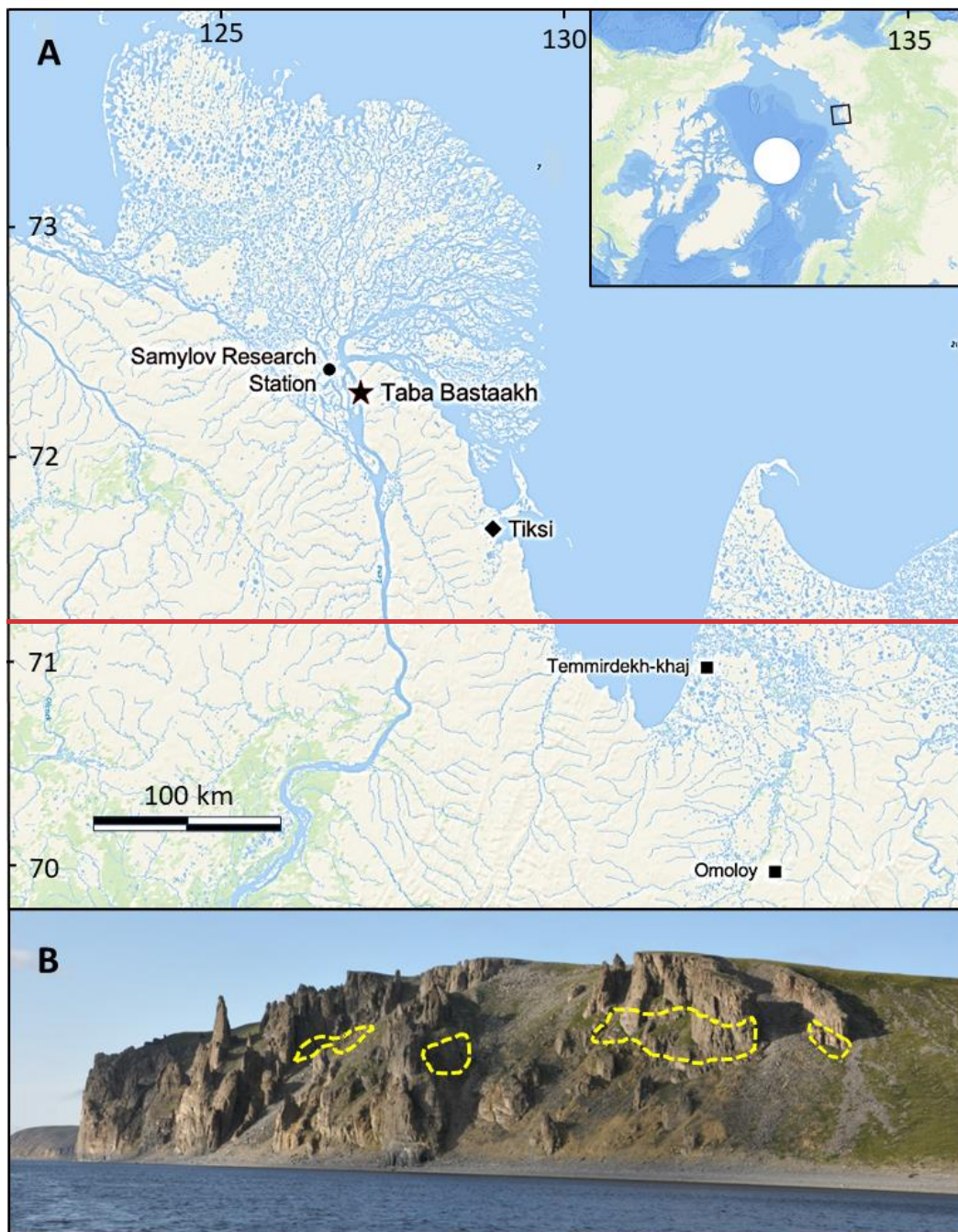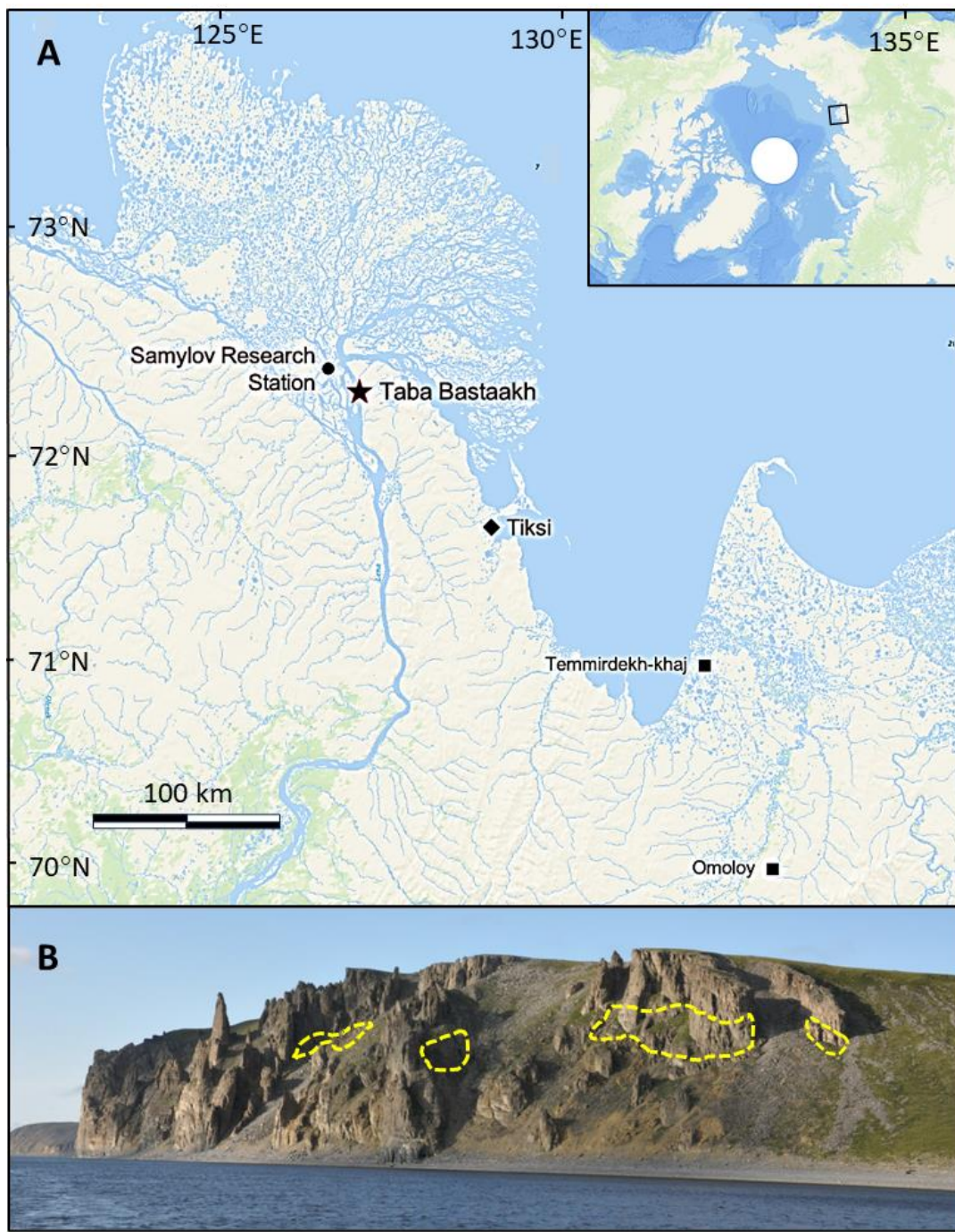
Figure 1: (A) Location of Taba Bastaakh sampling site, Samoylov Research Station, and relevant Miocene palaeoclimate reconstruction sites: Temmirdekh-khaj and Omoloy (Popova et al., 2012). The green shading shows forested areas (Map created in Esri ArcGIS), (B) Photograph of the Taba Bastaakh cliffs (height ca. 120 – 140 m) with cave locations outlined with yellow dashed lines (adapted from Vaks et al., 2024).

Meteorological data recorded at the Samoylov Island Research Station in the central Lena River Delta (N72.37°, E126.48°), ca. 20 km northwest of our study area, indicate a polar tundra climate (ET according to the Köppen-Geiger classification, Peel et al., (2007)), with a mean annual air temperature (MAAT) of -12.3°C, July average of +9.5°C, and February average of —

155 32.7°C (all temperature data averaged between 1998 and 2017) (Boike et al., 2019). ~~Mean~~ The closest available mean annual rainfall estimate is 309 mm (~~2002~~1980 - ~~2017~~2018), measured at the ~~-~~Tiksi meteorological station 90 km southeast of Taba Bastaakh~~is 169 mm and mean annual snow cover 0.3 m (Boike et al., 2019)~~.

2.2 Sample description

Fourteen speleothem samples were collected from the base of the Taba Bastaakh cliffs, on the bank of the Lena River in 2014.

160 ~~Today, t~~The modern caves are ice filled and inaccessible after a few meters, but erosion of the cliff face has exposed the interior of relic caves, ~~-~~with speleothems observed along the cliff walls. Observations of ongoing weathering of cave walls suggest that these samples originated from the cliff face 70-120 m above the sampling site where ~~-~~some in-situ speleothems were also found. All 14 samples have been ~~previously~~ dated to the Tortonian stage (Vaks et al., 2024 in review) using U-Pb dating following a modified method described in ~~(Vaks et al., 2020)~~ Vaks et al. (2020) and ~~-~~Mason et al. (2022)~~(Mason et al., 2022)~~.

165 The ^{235}U-^{207}Pb – ^{208}Pb/^{207}Pb isochron age of all samples yielded an age of 8.68 ± 0.09 Ma with a mean square weighted deviation of 1.2 (Vaks et al., 2024). Overlapping uncertainties of top and bottom ages allow only the construction of relative age-depth models along the growth profile of individual samples.

Four samples, STBB I – 1, STBB II – 7, STBB 4 – 2, and STBB 4 – 3 (Fig. 2) were selected for ~~further~~ this study, as their

170 high precision dates and large size make them amenable for coupled reconstruction of temperature and climate conditions at their time of deposition. All samples are composed of calcite (Vaks et al., 2024 in review).
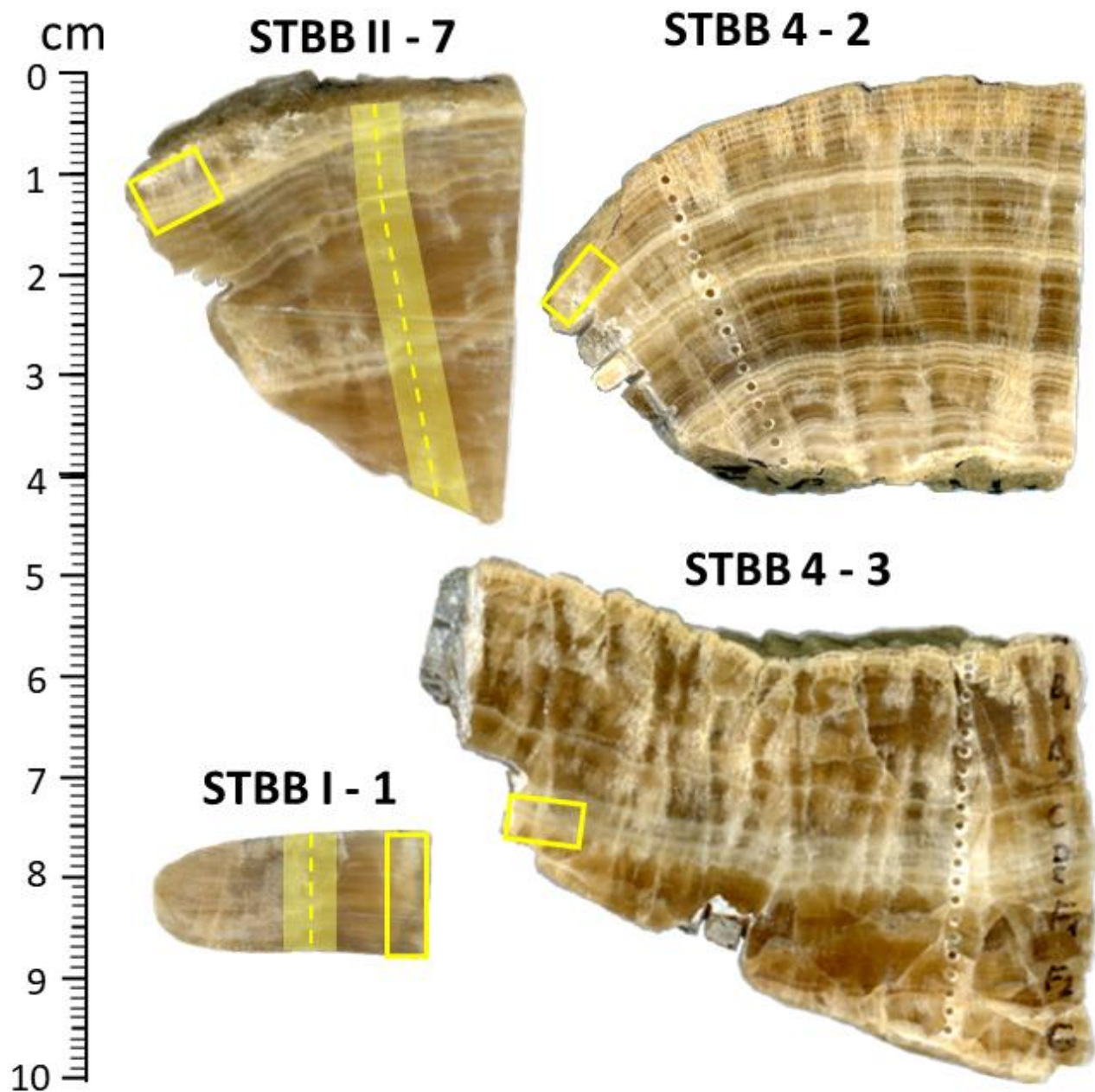
Figure 2: Speleothem samples used in this study. Thick translucent tracks, overlain with dashed lines, show the positions of stable isotope and trace element sampling profiles respectively (STBB I – 1 and STBB II – 7 only). Boxes indicate clumped isotope sampling positions.

3 Methodology

3.1 Clumped isotope geothermometry

Clumped isotope analyses for estimating speleothem formation temperatures were performed on subsamples of all four speleothems. Measurements were conducted at Northumbria University using a Nu Instruments Perspective dual inlet isotope ratio mass spectrometer coupled with an automated NuCarb preparation system. Samples were drilled from layers with well constrained ages and 325 ± 25 µg of powder loaded into sample vials, which were then evacuated, and reacted with concentrated orthophosphoric acid at 70°C. The reactant gas was dehydrated and cleaned using standard procedures (Petersen et al., 2015). Briefly, samples were dehydrated using two liquid nitrogen cryotraps, cooled to -80°C, and scrubbed of contaminants by passing through a 1 cm static trap filled with a Porapak™ Q (Waters Corporation) absorbent material, cooled to -30°C. Each replicate digestion was measured 40 times in dual inlet mode (total measurement time ca. 40 minutes). No pressure baseline correction was required.

Final clumped isotope (Δ_{47}) values were calculated using the software Easotope (www.easotope.org; John & Bowen, 2016) and the D47 Crunch Python package (Daëron, 2021). Both methodologies ~~using~~ used the IUPAC parameters for ^{17}O correction and isotopic ratios for VPDB and VSMOW (Bernasconi et al., 2018; Brand et al., 2010; Daëron et al., 2016). Application of both methods allowed Δ_{47} values to be inputted into both our in-house calibration, derived using Easotope, and the composite calibration of Anderson et al. (2021), which is derived using D47 Crunch.

For the Easotope method, ~~S~~sample Δ_{47} values were projected onto carbon dioxide equilibrium space (I-CDES-90) following the methodology of Dennis et al. (2011), using standards ETH1, ETH2, and ETH3, and I-CDES Intercarb Δ_{47} values from Bernasconi et al. (2021). Long term instrument performance was monitored with an internal standard, Pol-2 (a natural cave pool rim deposit), giving a long-term Δ_{47} external standard deviation of 0.032 ‰ ($\Delta_{47} = 0.656 \pm 0.003$ ‰ I-CDES-90, $T_{\Delta_{47}} = 2.4 \pm 1.0$ °C, N = 65).

Replicates were measured across multiple runs over a long period of time, similar to the sliding window approach employed by, e.g., Meinicke et al. (2020) and described by Daëron & Gray (2023). Stable isotope and Δ_{47} outliers ($> \bar{x} \pm 2\sigma$), alongside samples with elevated Δ_{48}, indicative of contamination (Eiler and Schauble, 2004), were discarded from final Δ_{47} calculations (Table S4). After pruning, a minimum of 14 replicate analyses were made for each sample such that Δ_{47} 95 % confidence intervals of ≤0.015 ‰ were achieved (i.e., ≤0.007 ‰ standard error). All Δ_{47} uncertainties are quoted as standard errors and 95% confidence intervals, according to best practices outlined by Fernandez et al. (2017).

For the D47 Crunch method, contaminated samples were pruned (identified by elevated Δ_{48} and Δ_{49}), alongside outlier ETH3 replicates ($> \bar{x} \pm 2\sigma$ for $\delta_{45} - \delta_{47}$) from each run. A linear drift correction was calculated for $\delta_{45} - \delta_{47}$ using ETH3 which was

then applied to all sample and standard data. Outlier ETH1, ETH2, and ETH3 ($> \bar{x} \pm 2\sigma$ for $\delta_{45} - \delta_{47}$) were then pruned from
each run before input into D47 Crunch to calculate I-CDES-90 Δ_{47} values. Stable isotope and Δ_{47} outliers ($> \bar{x} \pm 2\sigma$) were
pruned from the replicate data before final Δ_{47} calculations.

Clumped isotope temperatures ($T_{\Delta 47}$) were calculated using theby inputting D47 Crunch derived Δ_{47} values into the composite
regression of Anderson et al. (2021) and Easotope derived Δ_{47} values into an internal laboratory calibration derived calculated
from 17 natural inorganic calcite samples precipitated at known temperatures (Fig. S1, Tables S1 and S2). The derived
regression equation, calculated using the York least squares method (York et al., 2004) in the R geostats package, is:

$$\Delta_{47} = 0.0372 \ (\pm \ 0.0008) \cdot \frac{10^6}{T^2} + 0.166 \ (\pm \ 0.01) \tag{1}$$

Bracketed numbers denote one standard error. Thise in-house regression has a slightly lower gradient and higher intercept than
the composite regression derived by Anderson et al. (2021) (gradient = 0.0391 ± 0.0004, intercept = 0.154 ± 0.004).
Measurement and calibration uncertainties were propagated together to calculate Easotope temperature uncertainty according
tofollowing the methods of Huntington et al. (2009). D47 Crunch temperature uncertainties are the offset between
maximum/minimum possible temperatures and the central temperature estimate, calculated using the uncertainty in the
Anderson et al. (2021) regression and Δ_{47} standard errors.

3.2 Fluid inclusion analysis for temperature estimation

Fluid inclusion analyses were conducted on STBB I $-$ 1 and STBB II $-$ 7, where microscopic inspection confirmed the
presence of fluid inclusions. Measurements were performed at the University of Innsbruck, Austria following the method of
Dublyansky and Spötl, (2009). An aliquot of 1.5 g of carbonate was crushed in a heated crusher under He flow. The released
fluid inclusion water was cryo-trapped and then admitted into the TC/EA analyser (Thermo Scientific). After pyrolysis on
contact with glassy carbon at 1400°C, the evolved H_2 and CO were separated in the GC column and admitted to a Delta V
Advantage mass spectrometer (Thermo Scientific). Calibration was performed by measuring various amounts of reference
waters with isotopic compositions bracketing the expected compositions of the sample. Fluid inclusion isotope data are
reported with respect to. VSMOW. Accuracy of the measurement is 1.5 ‰ for δ^2H and 0.2 ‰ for $\delta^{18}O$.

Temperatures from fluid inclusions were calculated using the calibrations of (Tremaine et al., 2011) and (Coplen, 2007) for
water-calcite oxygen isotope fractionation.

3.3 Stable oxygen and carbon isotopes

Samples STBB I – 1 and STBB II – 7 were micromilled at 50 µm resolution along their growth length using a Sherline
micromill, following the methodology outlined in Lechleitner et al. (2020), producing a total of 225 and 823 subsamples,
respectively.

Stable isotope analysis was conducted at Northumbria University using a method adapted from Spötl & Vennemann, (2003). 110±10 µg of the sample was loaded into a 12 ml borosilicate exetainer tube, flushed with helium and reacted with concentrated orthophosphoric acid at 70°C. Liberated CO_2 was dried using a Gasbench II and analysed for carbon and oxygen isotope ratios. All samples were measured on a ThermoScientific Delta V Isotope Ratio Mass Spectrometer coupled with a ConFlo IV. We

245 used an in-house laboratory carbonate standard (Plessen), alongside international standards NBS18 and IAEA603, measured every 10 samples to evaluate the runs. An in-house carbonate standard (Pol-2) was used to evaluate long-term external standard deviation, achieving <0.1 ‰ for $\delta^{18}O$. All carbonate derived stable isotope data areis reported on the VPDB scale.

3.4 Trace element analysis

Trace element to calcium (X/Ca) ratios of 24 trace elements (tables S7 and S8) were measured along the stable isotope sampling

250 profiles of STBB I – 1 and STBB II – -7 at 2.6 µm resolution, using laser ablation inductively coupled plasma mass spectrometry (LA-ICP-MS) at the University of Western Australia following the methods outlined in Finestone et al. (2022).

We prioritised elements regularly utilised as hydrological proxies including Mg, Sr, and Ba (Stoll et al., 2012; Treble et al., 2015), alongside a vegetation proxy (P), indicators for detrital input (Al, Th) and heavy metals (Fe, Mn) associated with organic

255 matter binding (Hartland et al., 2012). See supplementary tables S7 and S8 for a full list of elements analysed. The stable isotope record was aligned to the trace element record using multiple visual markers such as prominent growth layers and surface blemishes.

We utilised pPrincipal component analysis (PCA) was utilised to identify common variability in the Taba Bastaakh trace

260 element records (Orland et al., 2014). A Gaussian kernel smoothing was applied to trace element records to remove missing data and minimise noise artefacts, before log transformation and z-score normalisation to account for the PCA's sensitivity to variable scaling. The PCA analysis was performed using the FactoMineR package in R. We applied spectral analysis to smoothed trace element and isotope records to reveal periodicities and dominant frequencies along the speleothem growth length.

265 3.5 Permafrost vulnerability modelling

We use our Miocene temperature reconstructions to update the Vaks et al. (in review) estimates of permafrost thaw vulnerability and the resultant potential carbon emissions if similar levels of warming were observed in the modern day. Using the 1991-2020 Global Historical Climatology Network (GHCN) land temperature dataset , we identified permafrost regions vulnerable to thaw under different warming scenarios. Following the approach of Vaks et al. (in review), we overlaid

270 vulnerable permafrost regions with modelled soil carbon content in the top 3 m of permafrost using QGIS to estimate potential soil organic carbon (SOC) emissions from the thawing region. Given the reconstructed warming from the Taba Bastaakh

275

4 Results

4.1 Clumped isotope temperature estimates

Clumped isotope results are summarised in Table 1. The Δ_{47} values of our samples range from 0.626 to 0.641 for the Easotope method and 0.640 to 0.656 for the D47 Crunch method, returning clumped isotope temperature ($T_{\Delta 47}$) estimates between 6.6

280 and 11.1°C, using our in-house calibration ($T_{\Delta 47\ Easotope}$) and 5.9 and 10.5°C for the D47 Crunch method and Anderson et al. (2021) regression ($T_{\Delta 47\ Crunch}$). Standard errorsUncertainty in Δ_{47} are is larger using the D47 Crunch method (standard error between 0.11 and 0.14‰, 95% confidence limits between 0.022 and 0.026 ‰) than the Easotope method (standard error between 0.06 and 0.07‰, 95% confidence limits between 0.012 and 0.015 ‰). This is expected given that D47 Crunch additionally propagates of the uncertainty associated with the normalisation standards (Daëron, 2021). This uncertainty is not

285 accounted for using Easotope. Both Easotope and D47 Crunch produce temperatures within uncertainty of each other, with higher $T_{\Delta 47}$ uncertainty in the D47 Crunch method due to larger Δ_{47} standard errors and the differing methods used to propagate calibration uncertainties (section 3.1).

between 0.006 and 0.007 ‰ (95% confidence limits between 0.012 and 0.014 ‰, translating to a temperature uncertainty of

290 < 2.4°C).

Table 1: Clumped isotope data and temperature estimates from Taba Bastaakh samples. N = number of replicate Δ_{47} measurements included in final Δ_{47} calculations, with the number of excluded samples in parentheses. See section 3.1 for uncertainty calculations. The fluid inclusion temperature (T_{FI}) from STBB I - 1 is presented for comparison with temperature range in parentheses. Replicate

295 measurement data is presented in Table S3.

Sample	N (Δ_{47})	Δ_{47} (‰, CDES90)	Δ_{47} SE (‰)	Δ_{47} 95% CI (‰)	$T_{\Delta 47}$ (°C)	$T_{\Delta 47}$ uncertainty (°C)	T_{FI} (°C) Tremaine	T_{FI} (°C) Coplen
STBB I - 1	21 (5)	0.626	0.007	0.015	11.1	2.1	9.0 - 19.2 (mean = 11.8)	10.9 - 21.5 (mean = 14.5)
STBB II - 7	18 (2)	0.641	0.006	0.012	6.6	1.8	NA	N/A
STBB 4-2	14 (3)	0.640	0.007	0.014	7.0	2.0	NA	N/A
STBB 4 - 3	14 (2)	0.634	0.007	0.014	8.7	2.4	NA	N/A

4.2 Fluid inclusion temperature estimate

Sample STBB I – 1 yielded 0.11 µL of fossil water with a $\delta^{18}O$ value of -17.5 ‰ VSMOW and a δD value of -127.7 ‰ VSMOW, giving a deuterium excess value (d-excess) of 12.3 ‰. This value lies within uncertainty of the modern Global

300 Meteoric Water Line (GMWL) (Craig, 1961), and ca. +9 ‰ in δ^2H above the modern Local Meteoric Water Line (LMWL) from the Samoylov Island Research Station (Spors, 2018) (Fig. S2). Since large sample volumes are required for fluid inclusion measurements, our $\delta^{18}O$ value is obtained from a speleothem section incorporating the entire growth length, representing an average of the entire speleothem. Thus, we applied a constant $\delta^{18}O$ value of -17.5 ‰ (VSMOW) for dripwater ($\delta^{18}O_{dw}$) across the entire calcite $\delta^{18}O$ record to obtain minimum and maximum temperature estimates. Sample STBB II – 7 failed to yield

305 sufficient inclusion water for analysis and thus no temperature estimate could be derived from this sample. The lower end of the STBB I – 1 fluid inclusion derived temperature estimate ($T_{FI} = 9.0 – 19.2°C$) overlaps with the independently derived $T_{\Delta 47}$ estimate ($T_{\Delta 47} = 11.1$).

310

Table 1: Clumped isotope data and temperature estimates from Taba Bastaakh samples. N = number of replicate Δ_{47} measurements included in final Δ_{47} calculations, with the number of excluded samples in parentheses. The number of sample replicates varies between methods due to different outlier exclusion methodologies and the exclusion of replicates with insufficient standard bracketing from the Easotope method calculations. All Δ_{47} values are reported on I-CDES90. The fluid inclusion temperature (T_{FI}) from STBB I – 1 temperature range is presented for comparison with the mean in parentheses. Replicate measurement data is presented in Table S3.

315

| | Easotope method | | | | | | D47 Crunch method | | | | | | Fluid inclusions | |
Sample	N	Δ_{47} (‰)	Δ_{47} SE (‰)	Δ_{47} 95% CI (‰)	$T_{\Delta47}$ (°C)	$\pm T_{\Delta47}$ (°C)	N	Δ_{47} (‰)	Δ_{47} SE (‰)	Δ_{47} 95% CI (‰)	$T_{\Delta47}$ (°C)	$\pm T_{\Delta47}$ (°C)	T_{FI} (°C) Tremaine	T_{FI} (°C) Coplen
STBB I – 1	21 (5)	0.626	0.007	0.015	11.1	2.1	25 (2)	0.643	0.011	0.022	9.6	6.0	9.0 – 19.2 (mean = 11.8)	10.9 – 21.5 (mean = 14.5)
STBB II – 7	18 (2)	0.641	0.006	0.012	6.6	1.8	14 (3)	0.640	0.013	0.025	10.5	6.5	NA	N/A
STBB 4 – 2	14 (3)	0.640	0.007	0.014	7.0	2.0	20 (1)	0.656	0.013	0.025	5.9	6.2	NA	N/A
STBB 4 – 3	14 (2)	0.634	0.007	0.014	8.7	2.4	16 (1)	0.647	0.014	0.026	8.5	6.6	NA	N/A

320

325

4.3 Stable oxygen isotopes

330   Speleothem $\delta^{18}O$ ranges between -17.5 and -14.6 ‰ VPDB, with mean values of -15.6 ‰ and -16.9 ‰ for STBB II – 7 and

STBB I – 1, respectively (Fig. 3). STBB I – 1 $\delta^{18}O$ exhibits an initial decline, reaching a minimum around 4mm where the

trend reverses. A sharp increase is observed around 7 mm where the record peaks and remains relatively constant thereafter.

The STBB II – 7 $\delta^{18}O$ record exhibits a similar initial decline of ca. 1 ‰ until ca. 20 mm, where this trend reverses. At ca. 37

mm $\delta^{18}O$ declines by ca. 1 ‰ in the final ca. 4 mm of the record.

335
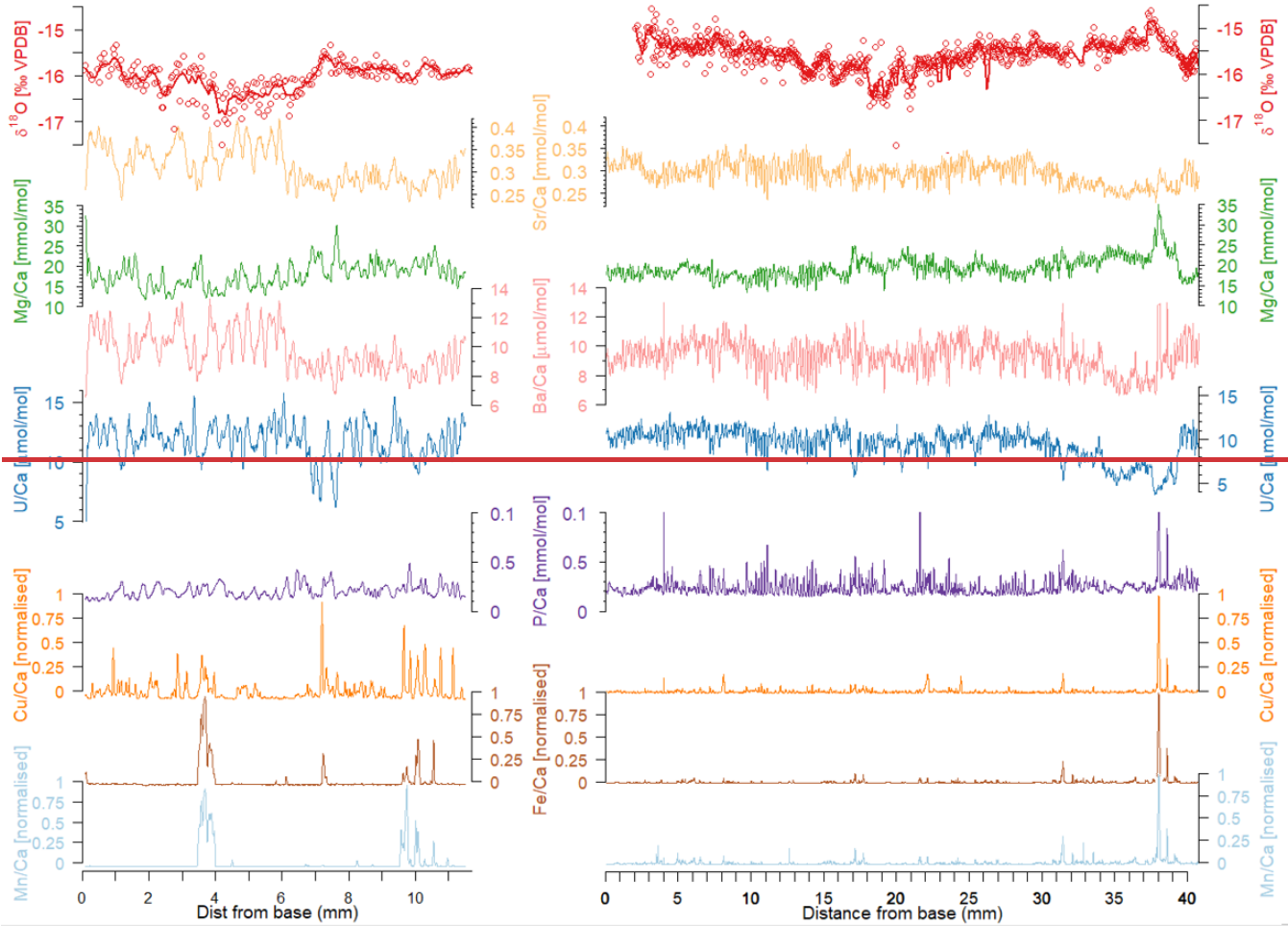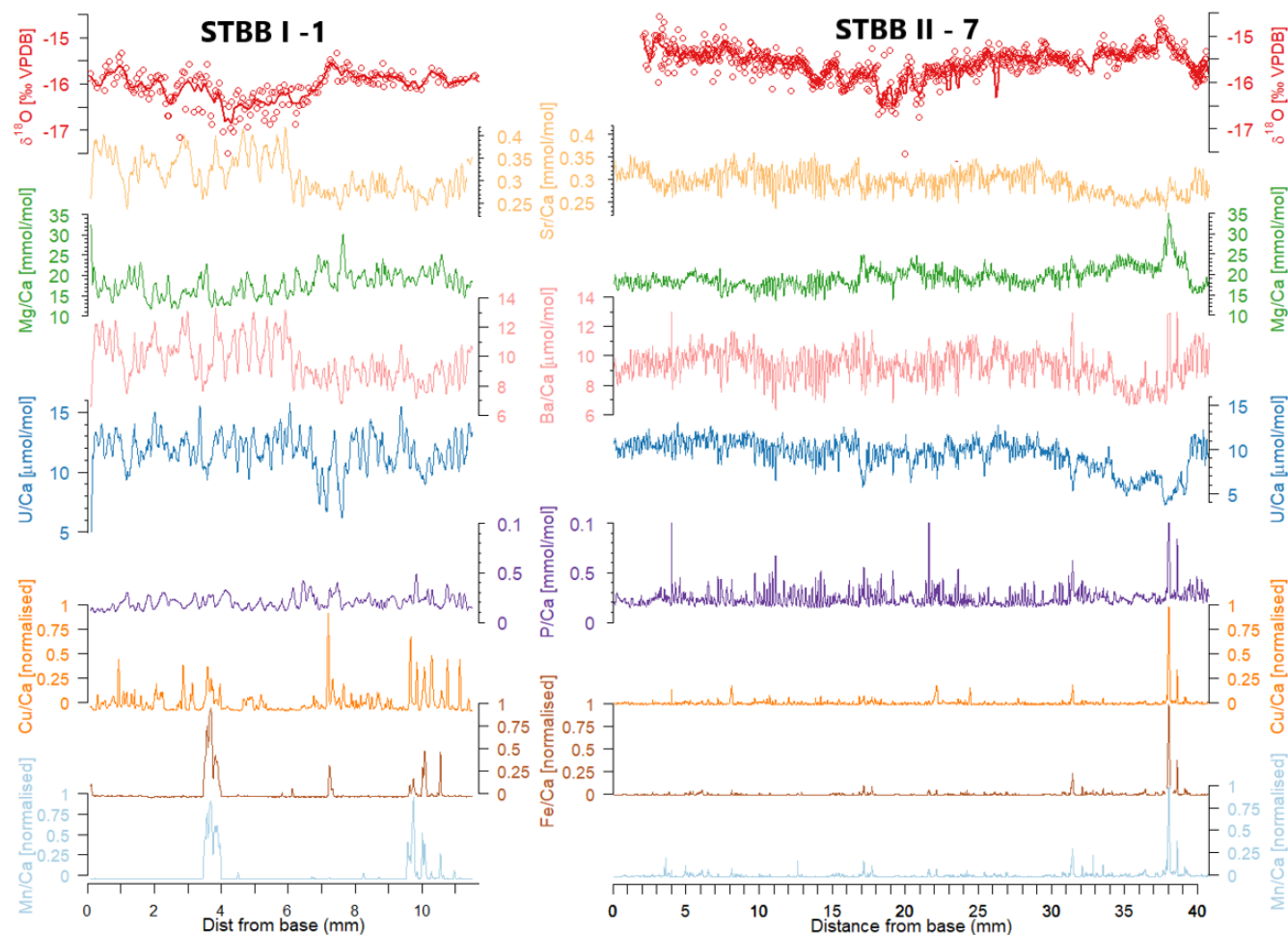
Figure 3: δ¹⁸O and selected trace element records for STBB I – 1 and STBB II – 7. δ¹⁸O data are shown with a 0.25 mm rolling window smoothing (thick lines). Trace elements are smoothed to 0.01 mm rolling window. Cu/Ca. Fe/Ca, and Mn/Ca ratios have been mean normalised for easier comparison between the two samples.

4.4 Trace elements

Our analysis focuses on 18 elements, predominantly cation substitutes Ba, Mg, Sr, U, and metals Cu, Co, Fe, and Mn. Concentrations of Y, La, Ce, Nd, Yb, and Th were below the detection limit and thus these elements were removed from subsequent analysis.

~~We utilised principal component analysis (PCA) to identify common variability in the Taba Bastaakh trace element records . A Gaussian kernel smoothing was applied to trace element records to remove missing data and minimise noise artefacts, before log transformation and z-score normalisation to account for the PCA's sensitivity to variable scaling. The PCA analysis was performed using the FactoMineR package in R.~~

We identify two dominant principal components (PCs) in each sample, accounting for 55.5 and 70.2 % of the variance in STBB I – 1 and STBB II – 7 respectively (Table 2, Fig. S3). ~~These PCs highlight two elemental groupings, t~~The first PC ~~is defined by correlations~~correlates with Ba, Sr, Mg, and U and accounts for 37 % of the variance in STBB I – 1 and 15.8 % in STBB II –– 7. These elements are commonly utilised as hydrological proxies in speleothems (Tooth and Fairchild, 2003; Treble et al., 2015) and we therefore refer to this PC as the hydrological PC. This PC also correlates with Na, P, and S in STBB I – 1. The second PC ~~is defined by correlations~~correlates with B, Fe, Mn, and Pb in both samples (Al, Cu, Co, Li, P, and Rb are also included in STBB II – 7) and accounts for 18.5 % of the variance in STBB I – 1 and 54.4 % in STBB II –– 7. These elements are commonly associated with detrital input via flushing (Hartland et al., 2012) and we therefore refer to this PC as the detrital PC herein.

360

~~We applied spectral analysis to the smoothed trace element and isotope records to reveal periodicities and dominant frequencies along the speleothem growth length. This~~ Spectral analysis revealed strong cyclicity in the hydrological PC elemental ratios (Ba, Mg, Sr, and U) in both samples, with dominant ~~frequencies~~wavelengths at ~ 0.3 mm and 0.5 mm in STBB I – 1, and 0.2 mm in the STBB II – 7 (Fig. S5). We also observe cyclicity in P (~ 0.3 mm and 0.5 mm in STBB I – 1, ~ 0.2 – 0.25 mm in STBB II – 7) and Cu (~0.2 mm, in STBB I – 1 only). Detrital PC metals remain relatively constant with sporadic spikes (Fig. 3).

Table 2: Results of multivariate principal component analysis on Taba Bastaakh speleothem samples. Two major elemental groupings are highlighted: The hydrological principal component, defined by elements Ba, Mg, P, Sr, U and the detrital principal component defined by elements Al, B, Cu, Co, Fe, Mn, Rb, Pb. An additional principal component (PC2) is identified in STBB I –– 1 but is not explored further.

STBB I –– 1			STBB II –– 7		
	% of variance explained	Elements		% of variance explained	Elements
Hydrological principal component	37	Ba, Cu, Mg, Na, P, S, Sr, U	Hydrological principal component	15.8	Ba, Mg, Sr, U
Detrital principal component	18.5	B, Fe, Mn, Pb	Detrital principal component	54.4	Al, B, Cu, Co, Fe, Li, Mn, P, Rb

5 Discussion

The late Miocene climate is widely accepted to have been several degrees warmer than today. Global SSTs were ca. 6°C warmer than present (Herbert et al., 2016) and mean global surface temperature was ca. 4.5°C above pre-industrial (1870-1900) (Pound et al., 2011). Most temperature estimates for the Miocene stem from marine sediments, and terrestrial data from

high northern latitudes are exceedingly sparse (e.g., Popova et al., 2012). Our speleothem records give a rare insight into terrestrial high latitude environmental changes, including temperature and hydrological conditions during this period.

Taba Bastaakh lies deep within the modern continuous permafrost zone with a MAAT of -12.3°C. ~~The regional~~We infer a ~~modern~~ mean annual ground temperature (MAGT) ~~of~~is -8.4°C, which we calculate by averag~~ing temperature~~ed along a 27 m borehole at the Samoylov Island Research Station (Boike et al., 2013). Since speleothem growth depends on liquid water supply, their presence at Taba Bastaakh indicates a much warmer climate at the time of their formation (8.68 ± 0.09 Ma).

5.1 Quantitative Tortonian temperature estimates

For comparison we calculated our clumped isotope temperatures using both the Easotope software and our in-house calibration, and the D47 Crunch data reduction algorithm with the composite calibration of Anderson et al. (2021). Both methods produce temperatures within uncertainty, giving confidence in our reconstructions. $T_{\Delta 47}$ uncertainty is greater for the D47 Crunch method due to propagation of the uncertainty in normalisation standards and the different method used to calculate calibration uncertainty (section 3.1).~~Our dataset allows for~~We also provide a direct comparison between clumped isotope and fluid inclusion-based temperature estimates on one sample (STBB I – 1), with the $T_{\Delta 47}$ estimate~~s~~ ($T_{\Delta 47 \text{ Easotope}}$ = 9.6 ± 6.0°C and $T_{\Delta 47 \text{ Crunch}}$ = 11.1 ± 2.1°C) overlapping with the T_{FI} estimates of both Tremaine et al. (2013) (9.0 – 19.2°C, mean = 11.8°C) (Table ~~3~~1) and Coplen et al. (2007) (10.9 - 21.5°C, mean = 14.5°C) calibrations (Table 1). A full discussion of temperature reconstruction uncertainties is given in the SOM. Herein we limit our discussion to temperatures derived using the Easotope method and our in-house calibration ~~which~~ since it is derived solely from subaqueous cave carbonates precipitated at temperatures similar to our samples. ~~This gives more conservative (i.e., lower) temperature estimates~~ Both methods give similar mean temperatures across all four samples (mean $T_{\Delta 47 \text{ Easotope}}$ = +8.4°C compared ~~to those based on the Anderson et al. calibration~~ with mean $T_{\Delta 47 \text{ Crunch}}$ = +8.6°C).

~~Anderson et al. (2021)Anderson et al. (2021)~~

~~We obtain quantitative estimates of Arctic temperatures at Taba Baastakh during the Tortonian between 6.6°C and 11.1°C, based on speleothem clumped isotopes and fluid inclusion isotopic analysis.~~ The large sample sizes required for clumped isotope analysis (ca. 4 mg) make sampling of individual growth layers impossible and thus our temperature estimates derive multi-annual means. The long-held assumption that cave temperature corresponds to mean surface temperature (e.g. Wigley & Brown, 1976) has been questioned (e.g. Domínguez-Villar et al., 2013). Cave temperature is impacted by numerous factors including ventilation (Pflitsch and Piasecki, 2003), thermal conductivity rates through the overburden (Domínguez-Villar et al., 2013), and vegetation and snow cover (Domínguez-Villar et al., 2013; Töchterle et al., 2024) which can all act to produce offsets of several degrees between surface and the cave environment.

410

Since erosion has mostly removed the Miocene overburden and brought our samples to the surface, it's impossible to know the full impact that ventilation and conduction may have had on the Taba Bastaakh cave temperatures. We suggest the insulating effects of winter snow and shading from summer vegetation likely counteracted each other with minimal overall effect. For instance, in cold regions, snow acts to insulate the ground, reducing heat loss to the atmosphere (Molnar, 2022).
415 This insulating effect has been shown to lead to cave temperatures 5-7°C higher than surface air temperatures in cold regions with persistent (ca. 233 days per year) snow cover (Töchterle et al., 2024). Our $T_{\Delta 47}$ reconstructions between 6.6 and 11.1°C suggest a mean annual surface temperature between modern day Stockholm (Moberg, 2021) and London (Met Office, 2024), which experience significantly less than 233 days of snow cover per year. We therefore envisage limited effect of snow insulation at Taba Bastaakh. In addition, there is palynological evidence that the Miocene treeline stretched as far north as
420 80°N (Steinthorsdottir et al., 2021b) and thus it is reasonable to assume a degree of forest cover at Taba Bastaakh during that time. Monitoring studies in Eagle Cave, Spain showed that transition from shrubland to forest resulted in a reduction in cave temperature up to 2°C due to changes in insolation and modification of soil properties (Domínguez-Villar et al., 2013). Given the higher latitude of Taba Bastaakh it would be reasonable to assume a reduced impact from insolation shielding compared with Eagle Cave however a small offset (< 2°C) is possible between our cave reconstructions and surface temperatures.

425

~~This effect appears to outweigh any impact of reduced continentality G~~given global average sea levels ca. 10 m higher during the late Miocene compared with modern (Miller et al., 2005), Taba Bastaakh might have occupied a more coastal position than the present day. In the modern Arctic, lingering summer sea ice can act to reduce coastal air temperatures compared with inland locations at the same elevation (e.g. Tuktoyaktuk and Inuvik in the Canadian Arctic (Hamma, 2022)) through increased
430 albedo and latent heat effects (Vihma, 2014). Miocene Arctic Sea ice was much reduced compared to the modern day (Stein et al., 2016) suggesting this effect may be limited. Nearby cold month temperature reconstructions from the coastal site Temmirdekh-khaj (Fig. 1) of between -2.8°C and + 1.1°C (Popova et al., 2012), considerably warmer than modern, support this notion, although we cannot rule out the possibility of lingering cold season sea ice reducing temperatures more than equivalent latitude inland locations.

435

~~Table 3: Comparison of Taba Bastaakh temperature estimates derived from different calibrations. $T_{\Delta 47}$ (this study) is compared with $T_{\Delta 47}$ derived from the composite calibration of Anderson et al. (2021). Anderson derived $T_{\Delta 47}$ uncertainties are calculated by~~
440 ~~propagating calibration uncertainties and Δ_{47} standard errors. T_{FI} is calculated using the calibrations of Tremaine et al. (2011) and Coplen (2007) with a constant $\delta^{18}O_{dw}$ of -17.5 ‰ (VSMOW) applied across the entire growth length.~~

Sample name	$T_{\Delta 47}$ (°C) This study	$T_{\Delta 47}$ Uncertainty (°C) This study	$T_{\Delta 47}$ (°C) Anderson	$T_{\Delta 47}$ Uncertainty (°C) Anderson	T_{FI} (°C) Tremaine	T_{FI} (°C) Coplen
STBB I-1	11.1	2.1	14.6	2.9	9.0–19.2 (mean = 11.8)	10.9–21.5 (mean = 14.5)
STBB II-7	6.6	1.8	10.1	2.2	N/A	N/A
STBB 4-2	7.0	2.0	10.5	2.3	N/A	N/A
STBB 4-3	8.7	2.4	12.1	3.1	N/A	N/A

For comparison we calculated our clumped isotope temperatures with both our in-house calibration (section 3.1) and the composite calibration of Anderson et al. (2021). $T_{\Delta 47}$ estimates derived using the Anderson et al. (2021) calibration are consistently higher than values derived from our own calibration by an average of 3.5°C (Table 3). We suggest that the steeper gradient (+0.0391 ± 0.0004) and lower intercept (0.154 ± 0.004) of Anderson et al. (2021) are influenced by five of their calibration samples formed at high temperatures (>252°C). Thus, we utilise our in-house calibration, which is derived solely from subaqueous cave carbonates precipitated at temperatures similar to our samples, for final temperature reconstructions. This gives more conservative (i.e., lower) temperature estimates compared to those based on the Anderson et al. calibration.

Our dataset allows for a direct comparison between clumped isotope and fluid inclusion-based temperature estimates on one sample (STBB I-1), with the $T_{\Delta 47}$ estimate (11.1 ± 2.1°C) overlapping with the T_{FI} estimates of both Tremaine et al. (2013) (9.0–19.2°C, mean = 11.8°C) (Table 3) and Coplen et al. (2007) (10.9–21.5°C, mean = 14.5°C) calibrations. A full discussion of temperature reconstruction uncertainties is given in the SOM.
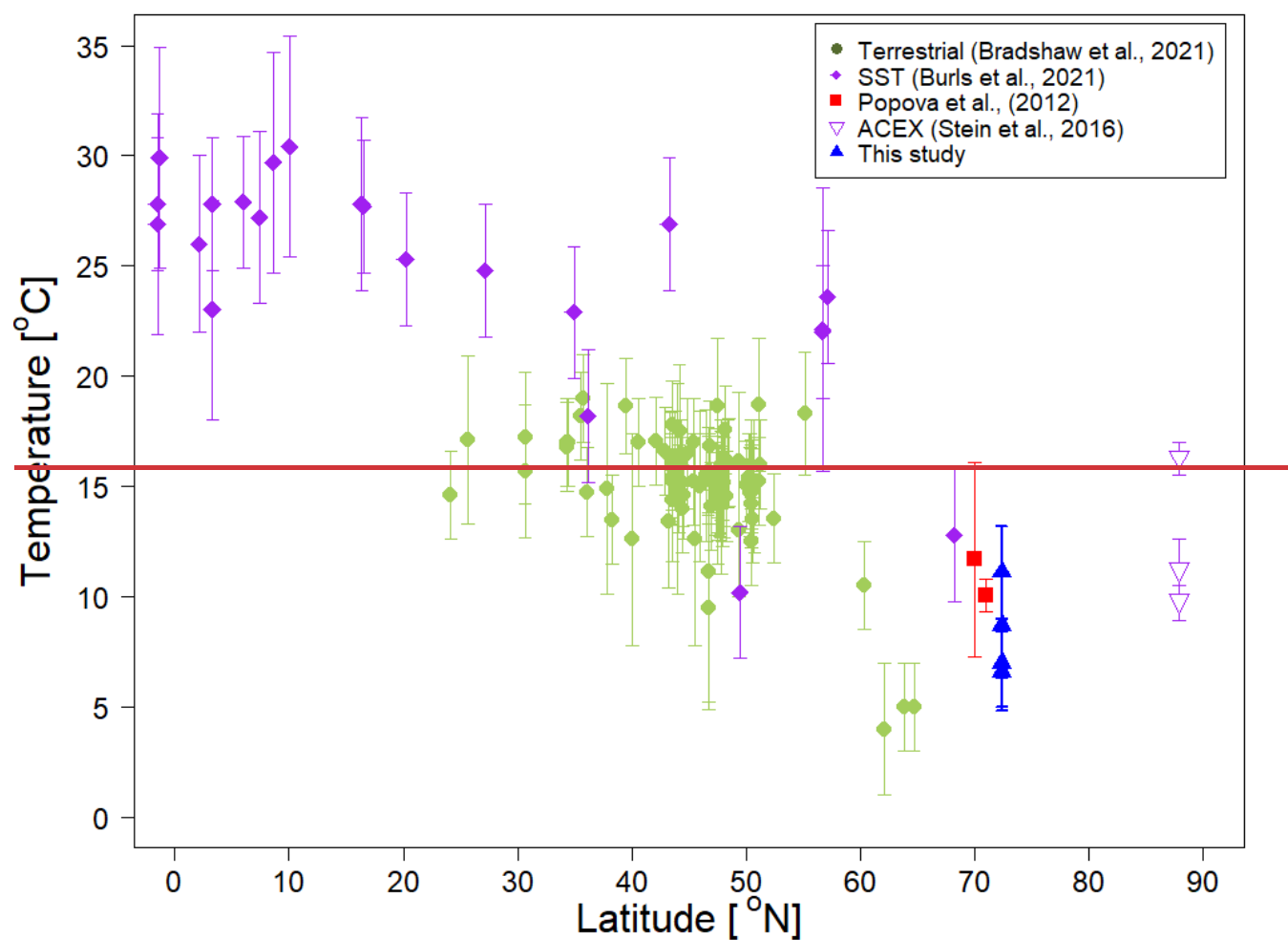
455
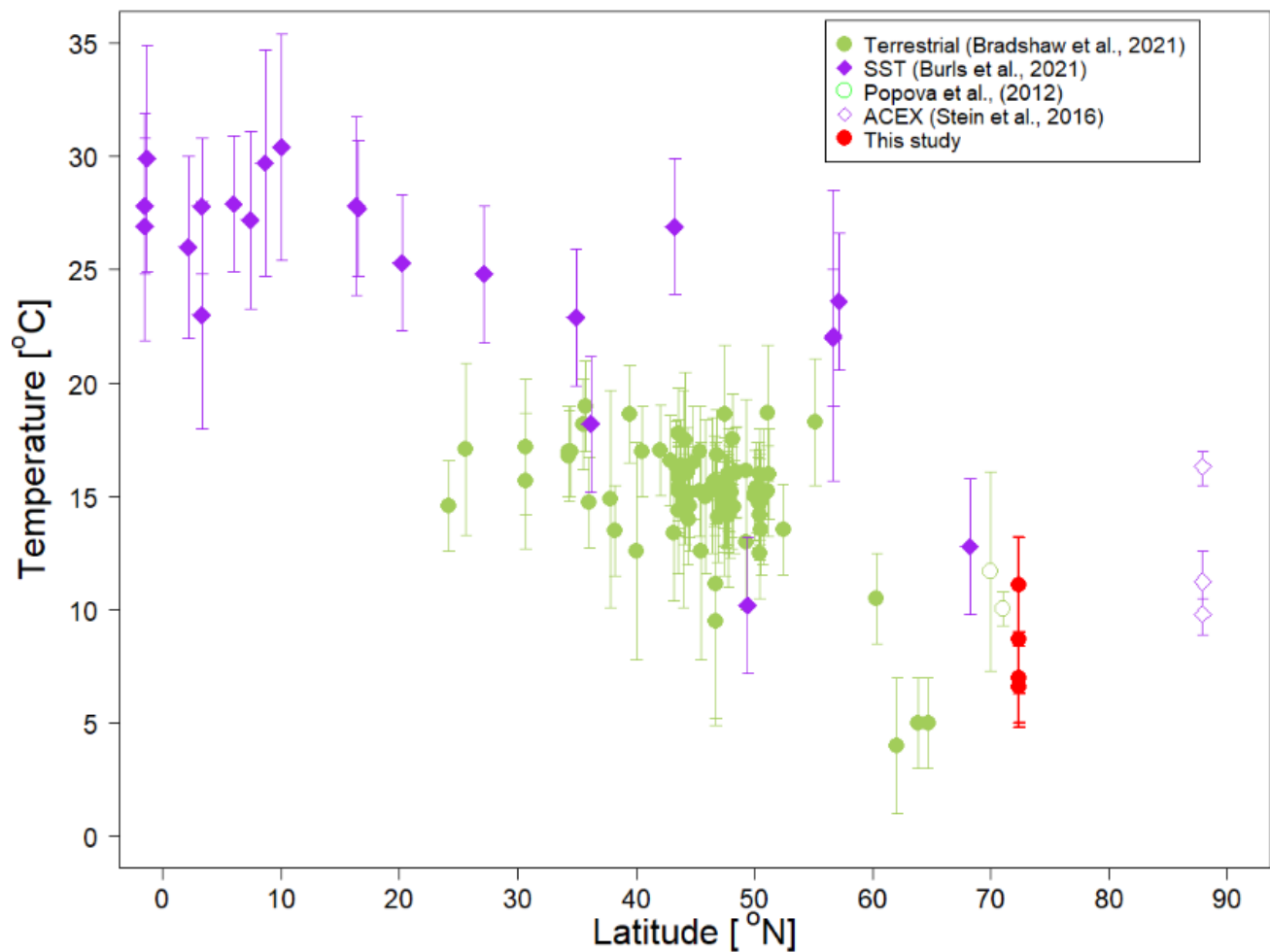
Figure 4: Compiled Northern Hemisphere late Miocene temperature reconstructions. Green ~~filled~~ circles are Tortonian terrestrial mean annual temperatures reconstructions from the Bradshaw et al. (2012) database with additional sites Temmirdekh-khaj and Omoloy from Popova et al. (2012) shown ~~as red squares~~unfilled. Error bars for terrestrial reconstructions show minimum and maximum estimates. The late Miocene SST dataset from Burls et al. (2021) is shown as purple diamonds with error bars showing uncertainty in reconstruction estimate. Additional SST estimates from the ACEX borehole are shown as unfilled purple ~~triangles~~ diamonds (Stein et al., 2016). ACEX borehole temperatures show the average of the four different Alkenone derived temperature calibrations quoted in Stein et al. (2016), with error bars showing the maximum, and minimum values. Both terrestrial and SST datasets have been filtered to show only data with age uncertainties overlapping our Taba Bastaakh estimates. The ~~blue~~ red ~~triangles~~ circles are the four Taba Bastaakh clumped isotope temperature reconstructions from this study.

To our knowledge, the Taba Bastaakh temperature reconstructions are the most northerly terrestrial Tortonian MAAT estimates to date and support the consensus of a reduced latitudinal temperature gradient during the late Miocene (Burls et al., 2021; Gaskell et al., 2022). Our temperature estimates agree well with independent high latitude temperature reconstructions (Fig. 4). Late Miocene fossil pollen assemblages from nearby sites Temmirdekh-khaj (132°E, 71°N) and Omoloy (133°E, 70°N) (Fig. 1) yield MAAT estimates between 7.3 and 16.1°C (Popova et al., 2012). The same authors infer a late Miocene MAAT

of 9.7°C for the whole of eastern Siberia. Exceptionally high summer SSTs between 10 and 16°C have been reconstructed for the Arctic Ocean at the Lomonosov Ridge (88.5°N) (Stein et al., 2016). Our temperature reconstructions provide new evidence of a terrestrial MAAT ca. 18 to 23°C warmer than terrestrial present in the Siberian Arctic during the Tortonian. This is far in excess of negative temperatures simulated by models of in the Alaskan Arctic during the Middle Miocene (Goldner et al., 2014)

475 and the ca. 3.5°C above present day zonal mean estimated in general circulation modelling of the Tortonian (Micheels et al., 2007). and the 70°N zonal mean during the late Miocene . Thus, our findings confirm the long-established discrepancy between model simulations and proxy reconstructions with the most northerly terrestrial Miocene proxy temperature record to date, and suggests that Miocene Arctic amplification is not accurately captured by general circulation models.

480 Since Tortonian global mean surface temperature of 4.5°C above pre-industrial (Pound et al., 2011)) was similar to the 2 – 5°C projected for the end of the century projections under high emissions scenarios (Masson-Delmotte et al., 2021), our findings provide estimates for end-of-century Arctic temperature amplification and precipitation variability under high emissions scenarios extreme levels of anthropogenic warming. Our estimates are considerably higher than the ca. 10 - 12°C of Arctic warming by the end of the century projected in modelling studies (Nazarenko et al., 2022; Xie et al., 2022). (Overland

485 et al., 2019) Our exceed and exceed s reconstructions for the middle-Pliocene Warm Period (3.3 - 3.0 Ma) which suggested Arctic surface air temperature warming of 7.2°C given global mean temperatures 3.2°C above pre-industrial (de Nooijer et al., 2020).

Our estimates provide useful constraints on near-future Arctic warming, but we emphasise that different planetary scale

490 boundary conditions in the Miocene compared with today mean our deep-time reconstructions provide imperfect analogues for anthropogenic warming. Whilst the Miocene marked a large-scale expansion of global ice sheets, both northern and southern hemisphere ice sheets were highly dynamic, particularly in Greenland which was likely only partially glaciated (Steinthorsdottir et al., 2021b). Evidence from ice-wedge pseudomorphs suggests the onset of high-latitude Northern Hemisphere permafrost formation occurred in the late Pliocene (~3 Ma) (Opel et al., 2025) and it is very likely that the Northern

495 Hemisphere was permafrost-free during the Tortonian (Vaks et al., 2024 in review). These, and other, slow planetary-scale feedbacks will have played a major role in the Miocene global energy budget that are unlikely to be of similar significance in driving near future temperatures.

500 (Miller et al., 2005)
at a time when global mean temperature was ca. 4.5°C warmer than pre-industrial . This Arctic amplification estimate is considerably higher than existing model .of ca. 10 - 12°C Arctic warming by the end of the century under high emissions scenarios .
(Goldner et al., 2014)(Micheels et al., 2007)(Pound et al., 2011)(Masson-Delmotte et al., 2021)

5.2 Stable oxygen isotope records

Both Taba Bastaakh speleothem δ^{18}O records show very negative values (means: -15.6 ‰ and -16.9 ‰). Modern studies have shown that dripwater δ^{18}O (δ^{18}O$_{dw}$) predominantly reflects changes in δ^{18}O of precipitation (δ^{18}O$_p$) above a cave (Baker et al., 2019) which, at high latitudes, is largely driven by temperature (Dansgaard, 1964). Monthly mean values of δ^{18}O$_p$ from both the Samoylov Island Research Station (2013-2017) and Tiksi (2004-2017) are highly correlated to mean monthly air temperatures (Spors, 2018). Thus, we interpret δ^{18}O$_p$, and in turn δ^{18}O$_{dw}$ and speleothem δ^{18}O, as indicative of temperature variations at Taba Bastaakh.

Similarly negative δ^{18}O values (ca. -16 to -11 ‰) are found in Greenland speleothems during Marine isotope stage (MIS) 15a – 14 (Moseley et al., 2021), a middle-Pleistocene period of unusually warm and prolonged interglacials (Rodrigues et al., 2011; Hao et al., 2015). Holocene Arctic speleothem reconstructions are absent from the literature; however, the Taba Bastaakh isotope records agree well with modern Holocene values found in central Siberia 15-20 degrees latitude faurther south at Botovskaya Cave (55°N), Okhotnichya Cave (52°N) (ca. -18 to -13 ‰) (Lechleitner et al., 2020), and Kinderlinskaya Cave (54 °N) (ca. -14 to - 11 ‰) (Baker et al., 2017). We note that the more negative δ^{18}O of the Miocene Ocean may have compounded a shift to more negative δ^{18}O values (Westerhold et al., 2020), but this would have been somewhat offset by reduced continentality at Taba Bastaakh (generally associated with positive shifts in δ^{18}O) given the ca. 10 m higher global sea level (Miller et al., 2005). Given these competing influences we do not propose any firm assertions on the impact source values of δ^{18}O compared with the modern day on the δ^{18}O signal. Thus, we assume that the stable oxygen isotope records from Taba Bastaakh support the independent temperature estimates of , suggesting mucha much higher MAAT during the Tortonian than at present.

5.3 δ^{18}O signal of palaeo-dripwater

We estimate δ^{18}O$_{dw}$ by using the clumped isotope derived temperatures in the temperature dependent water-calcite oxygen isotopic fractionation relationship from Tremaine et al. (2011) (Table 3). Given the control of δ^{18}O$_p$ on δ^{18}O$_{dw}$, the latter provides an estimate for δ^{18}O$_P$. Due to the large sample sizes required for clumped isotope analysis, the samples integrate multiple growth layers and therefore δ^{18}O$_{dw}$ values reflect multi-annual means.

δ^{18}O$_{dw}$ ranges between -17.6 ± 0.4 ‰ and -18.4 ± 0.4 ‰ (VSMOW), within error of the fluid inclusion measurement from STBB I – 1 (-17.5 ± 1.0 ‰). Agreement between these two independent δ^{18}O$_{dw}$ derivations provides additional confidence in our estimate. We stress that this assessment does not consider the influence of additional post-precipitation evaporative processes that complicate isolation of a pure precipitation signal from speleothem fluid inclusions (Lachniet, 2009).

Assuming $\delta^{18}O_{dw}$ reflects $\delta^{18}O_p$, oOur reconstructed ~~Lena Delta~~ $\delta^{18}O_p$ values for the Tortonian suggest a mean annual precipitation regime between the modern summer (-15.9 ‰) and autumnal regimes (-19.1 ‰) (modern annual mean = -21.6 ‰) (Bonne et al., 2020) .

Table 3: Dripwater isotopic composition estimates for the four Taba Bastaakh speleothems. $\delta^{18}O_{cc}$ is the $\delta^{18}O$ of calcium carbonate. $\delta^{18}O_{cc}$ uncertainties are standard errors. $\delta^{18}O_{dw}$ uncertainty is calculated from propagation of $T_{\Delta47}$ and $\delta^{18}O_{CC}$ uncertainties.

Sample	$T_{\Delta47}$ (°C)	$\delta^{18}O_{cc}$ (‰, VPDB)	$\delta^{18}O_{dw}$ (‰, VSMOW)	$\delta^{18}O_{FI}$ (‰, VSMOW)
STBB I – 1	11.1 ± 2.1	-16.02 ± 0.01	-17.6 ± 0.4	-17.5 ± 1.0
STBB II – 7	6.6 ± 1.8	-15.86 ± 0.01	-18.3 ± 0.4	
STBB 4 – 2	7.0 ± 2.0	-16.01 ± 0.01	-18.4 ± 0.4	
STBB 4 – 3	8.7 ± 2.4	-15.87 ± 0.01	-17.9 ± 0.5	

5.4 Seasonal hydrological regime

We propose that the cyclical behaviour of trace elements is driven by a strong seasonal hydrological regime at the time of speleothem deposition. The identified hydrological PC groups in both STBB I – 1 (PC1) and STBB II – 7 (PC2) are associated with element ratios widely utilised as hydrological proxies: most commonly Mg/Ca, Sr/Ca and Ba/Ca (e.g., Tooth & Fairchild, 2003; Treble et al., 2015). These alkali metals are transported via dripwaters and substituted into the carbonate lattice during speleothem deposition. In periods of low throughflow, Ca is preferentially removed from dripwaters through prior carbonate precipitation (PCP), increasing relative concentrations of Mg, Sr, and Ba.

Correlation of Sr and Mg is often used as an indicator of ~~prior carbonate precipitation~~ (PCP) from infiltration waters before they reach the speleothem formation site (Wassenburg et al., 2020). Sr/Ca and Mg/Ca exhibit no consistent relationship in either Taba Bastaakh sample, with periods of high correlation interspersed with periods of no correlation (Fig. S4). Deviation from constant Mg/Ca vs Sr/Ca ratios can arise from growth rate variability (Sliwinski et al., 2023) and changing mixing ratios of dripwater solutions derived from multiple geological endmembers (Tremaine and Froelich, 2013). Dating constraints hinder identification of growth rate variability in the Taba Bastaakh records, however Sr/Ca and Mg/Ca decoupling could arise from periods of hydrological rerouting or changing endmember dissolution rates between the carbonate and the overlying dolomitic limestone (Izokh and Yazikov, 2017) altering Mg/Ca concentration input.
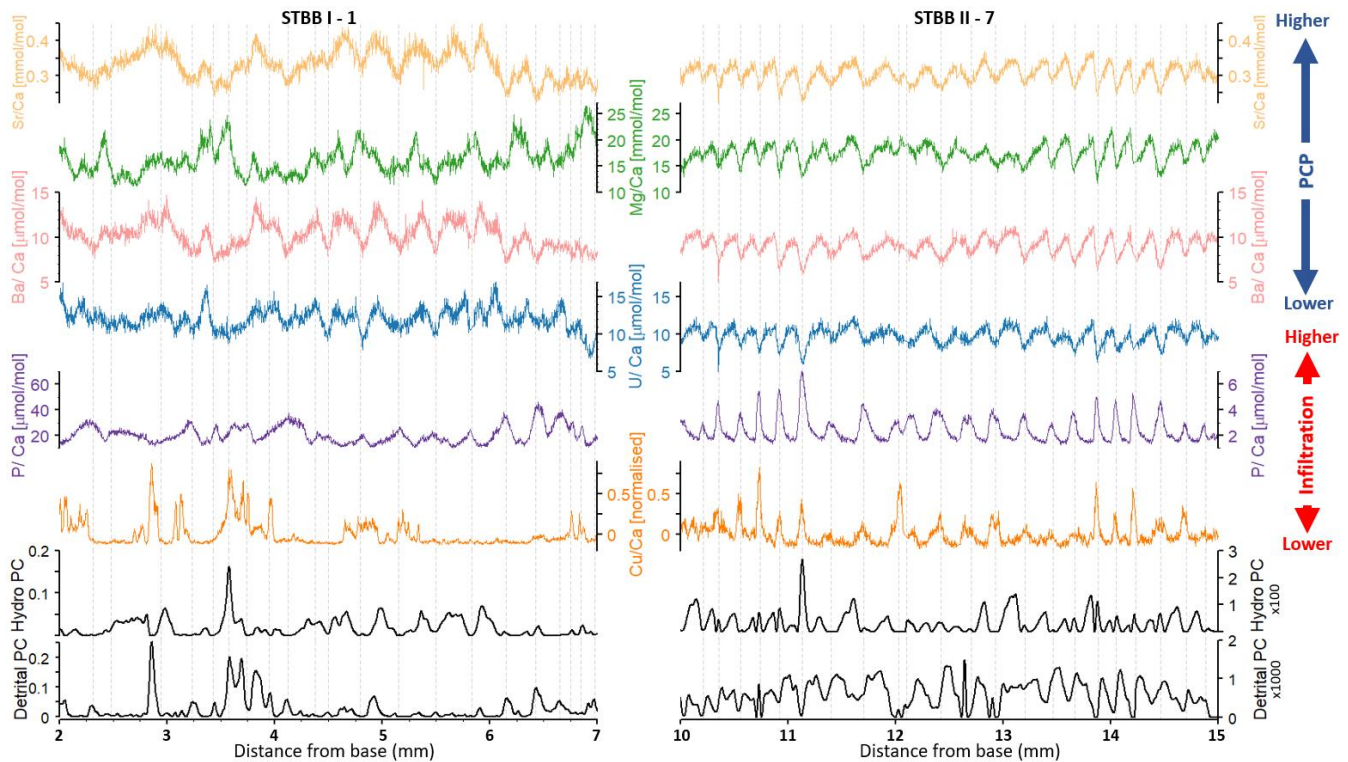
Figure 5: High resolution trace element concentrations, and major principal components along the STBB I – 1 and STBB II – 7 sampling profiles. Cu/Ca ratio has been mean-normalised for easier comparison between the two samples. Grey dashed vertical lines mark the positions of Sr/Ca troughs.

Tremaine and Froelich (2013) showed that in order to diagnose Mg/Ca and Sr/Ca as reliable 'wet vs. dry' proxies, Sr/Mg must remain constant along the entire sampling profile. Whilst this is not the case in the Taba Bastaakh records, Sr/Ca is remarkably highly correlated with Ba/Ca (r = 0.98, p-value < 0.01 in STBB I – 1 and r = 0.55, p-value < 0.01 in STBB II – 7) and U/Ca (r = 0.59, p-value < 0.01 in STBB II – 7 and r = 0.83, p-value < 0.01 in STBB II – 7) along the entire growth length of both Taba Bastaakh samples (Figs. S3 and S4). Ba/Ca has been extensively utilised as a PCP proxy (e.g. Stoll et al., 2012) and might constitute a more robust PCP proxy that is less likely affected by host rock composition at Taba Bastaakh. Fewer studies have considered U/Ca as potential indicator of infiltration changes. Dripwater U is derived from bedrock dissolution and is readily incorporated into the calcite lattice (Oster et al., 2023) . The strong correlation of U with both Sr and Ba in the Taba Bastaakh records suggests that U/Ca may also reflect changes in PCP in the Taba Bastaakh records. Finally, P/Ca is also included in the hydrological principal component in STBB I – 1, and is strongly anticorrelated with Sr, Ba, and U. P is scavenged from infiltration water during calcite precipitation, thus decreasing P/Ca in dripwater during periods of elevated PCP (Johnson et al., 2006) — as is observed in the Taba Bastaakh records (indicated by elevated Sr/Ca, Ba/Ca and U/Ca, Fig. 5).

The detrital principal component is characterised by metals which are commonly associated with organic matter flux into the
cave (Hartland et al., 2012). These metals are poorly soluble and colloidally transported through organic matter binding during
soil infiltration (Hartland et al., 2012). Hartland et al. (2012) demonstrated Cu and Co organic binding by showing speleothem
Cu/Ca vs Co/Ca ratios in line with those predicted based on n1 NICA-Donnan humic and fulvic binding affinity ratios (Milne
et al., 2003). We repeat this calculation for our records and find that the measured Cu/Ca vs Co/Ca ratios show good agreement
with predicted ratios in STBB II – 7 (Fig. S5), confirming these metals are indeed derived from organic binding in this sample.
There is poor agreement between predicted and measured ratios in STBB I – 1 suggesting detrital metals in this sample are not
associated with organic binding. Phosphorus is also included in the detrital principal component in STBB II – 7. P supply has
been linked with vegetative leaching during storm events (Pionke et al., 1997) with maximum P/Ca linked to elevated
infiltration rates (Borsato et al., 2007). Thus, the strong positive correlation observed between P and organically ~~binded~~ bound
metals provide~~s~~ further evidence that these element variations are reflecting infiltration rates in STBB II – 7.

We present a subsection of the trace element records in Fig. 5 where correlation between Mg and other hydrological proxies
is highest to illustrate the relationship between hydrological and detrital proxies. In STBB II – 7, maxima in PCP controlled
elements Sr, Mg, Ba and U coincide with minima in the infiltration-controlled elements P and Cu. Thus, wet seasons are
identified as maxima in infiltration proxies (Cu/Ca and P/Ca), and minima in the PCP proxies Sr, Mg, Ba, and U. The opposite
is true for dry seasons. The relationship between detrital infiltration and PCP proxies is less apparent in STBB I – 1 (Fig. 5),
where we have demonstrated that detrital proxies are not controlled by organic matter influx (Fig. S5). However, strong
cyclicity is observed in all PCP proxies, as well as P, which shows a similar anticorrelation with PCP proxies as in STBB II –
7.

Spectral analysis ~~displays~~ reveals dominant ~~trace element~~ cycles corresponding to distances of 0.3 and 0.5 mm and 0.2 mm in
STBB I – 1 and STBB II – 7 respectively (Fig. S6). Our assertion that these cycles are annual is supported by the observed
alignment of the Sr/Ca record with annual banding in STBB II – 7 (Fig. S7), identified by changes in the visual greyscale. We
use the free ImageJ software to extract ~~greyvalues~~ grey values (the intensity of light carried in a single pixel) along the growth
length of a high-resolution composite image STBB II – 7 thin sections (Breitenbach and Marwan, 2023). In this way, annual
growth bands were identified. Sr/Ca peaks coincide with greyscale peaks (brighter layers). Thus, our trace element periods
reflect growth rates of 200 µm (STBB II ~~–~~ 7) and 300 µm (STBB I ~~–~~ 1) a year, similar to those observed in modern temperate
regions (Johnson et al., 2006; Sherwin and Baldini, 2011).

We compare Miocene and modern-day hydrological seasonality using a 20-year instrumental record of ~~precipitation~~ rainfall
from the nearby Samoylov Island Research Station. We combined common hydrological proxies Sr/Ca, Ba/Ca, U/Ca, Mg/Ca,
and P/Ca to obtain a single representative proxy-stack-average timeseries and aligned it to the instrumental record using
dynamic time warping (Berndt & Clifford, 1994) (See SOM for details, Fig. S8). While this methodology does not eliminate

the considerable challenges of comparing palaeoseasonal proxy data to modern seasonality, it yields a pseudo-seasonal time axis that allows us to estimate precipitation seasonality in a comparable fashion for both sets of records. We compared the aligned modern and Miocene hydrological seasons using a spectral seasonality measure. Precipitation seasonality is quantified by the total spectral power $|P|_s$ summed over the spectral band that closely encapsulates the seasonal peak (Fig. S9). Higher power in the seasonal band is interpreted as a more pronounced/stable seasonal signal. Detailed methodology is given in the supplementary materials.

The combined hydrological proxy records suggest a stronger seasonal precipitation regime during the Tortonian (i.e. a more pronounced seasonal cycle) compared with modern day conditions (Fig. 6). This is true of both samples, with significantly higher median spectral power in the seasonal band in the Miocene compared with the modern. We recognise the limitations in the modern record which, whilst the closest available modern precipitation timeseries, measures only the liquid fraction and not snowfall, which constitutes ca. 30% total precipitation at the Samoylov Research Station (Boike et al., 2013). However, exclusion of the winter snow component within the modern record will create an apparent stronger seasonal contrast. Given that our Tortonian hydrological proxy record exhibits a stronger seasonality measure than this modern rainfall record, we argue this reinforces our finding of a more seasonal hydrological regime in the Tortonian.
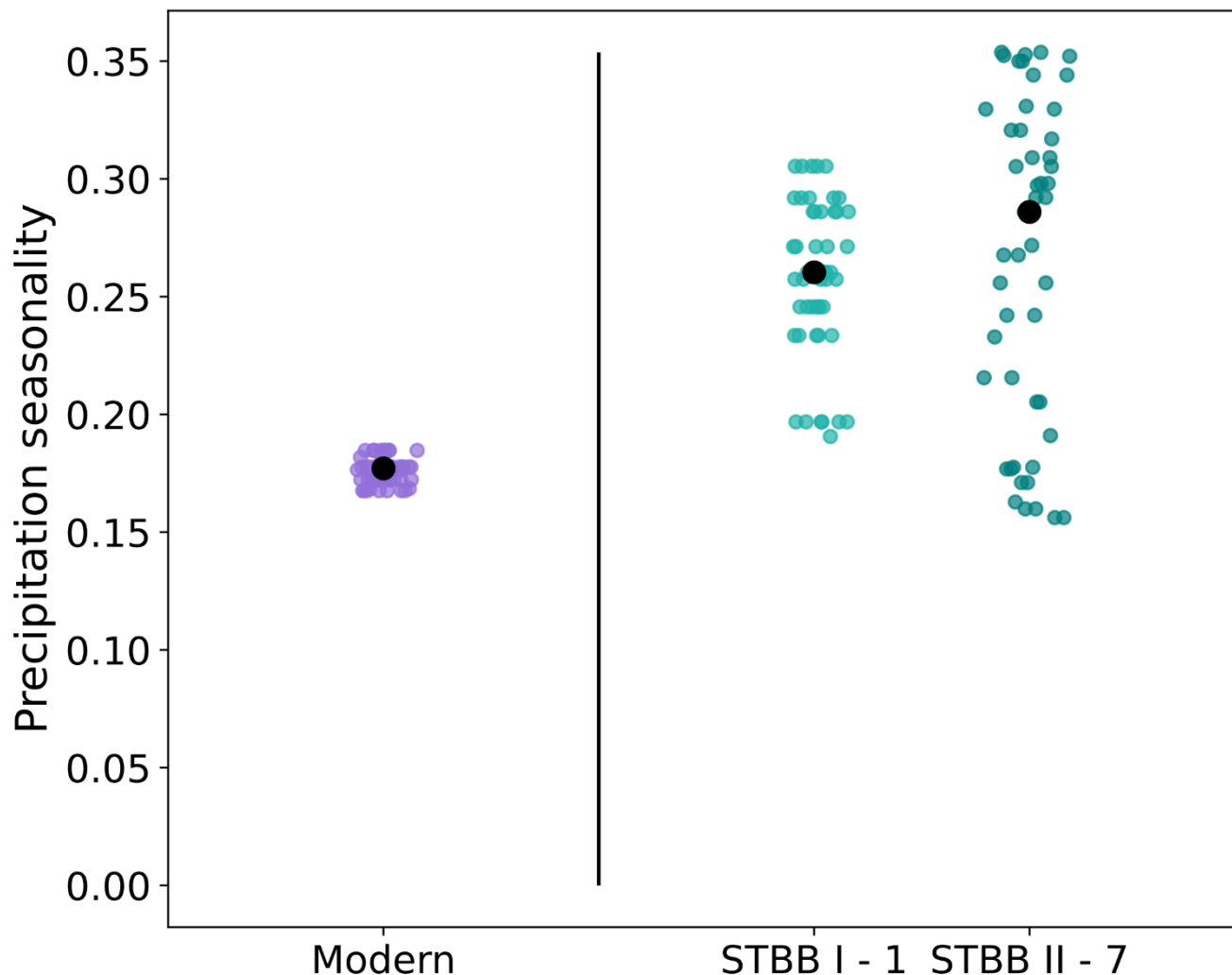
630 Figure 6: Reconstructed precipitation seasonality ($|P|_s$ summed over the seaonal peak spectral band) in Tortonian samples STBB I – 1 and STBB II – 7, compared with the modern day. An alignment procedure based on dynamic time warping allows for their comparison. Coloured points show seasonality values for different widths of the seasonal band between 0.2 (0.9 - 1.1) and 0.5 (0.75 - 1.25). Black points show the median over all values. Both samples show overall enhanced seasonality in the Miocene compared with the modern day.

635

Numerous studies have suggested the Miocene was a time of enhanced seasonality in the mid latitudes with warm-wet, cold-dry seasonal cycles in central Europe (Bruch et al., 2011; Harzhauser et al., 2011). At high latitudes, the picture is less conclusive. Pollen reconstructions from eastern Siberia suggest the late Miocene marks the onset of modern atmospheric circulation patterns and the establishment of today's wet summer/dry winter regime, albeit with considerably higher total

640 precipitation between 700 mm and 900 mm per year (Popova et al., 2012). At Temmirdekh-khaj and Omoloy, Miocene pollen reconstructions suggest the mean annual range in precipitation (the difference between wet and dry season amplitude) was 70

- 80 mm and 110 - 130 mm respectively. This seems large compared with today's mean ~~annual~~ summer precipitation of 169 mm and annual precipitation of 309 ~~but~~mm but should be viewed in context of a ~~likely~~ wetter Tortonian regime given higher moisture availability from a summer ice-free Arctic (Stein et al., 2016). Analysis of fossil wood δ^{13}C from Cherskiy (N67.7°, E161.6°) in northeastern Siberia shows a high variability in precipitation, with the wet season alternating between summer and winter (Schubert et al., 2017). In contrast, our Taba Bastaakh records suggest an enhanced seasonal precipitation regime compared with the modern day. We propose this likely arose from differing moisture availability from the nearby Arctic Ocean which was largely sea-ice covered during the Tortonian winter and ice-free during Tortonian summers (Stein et al., 2016). This would have led to enhanced evaporation and moisture transport into northern Siberia in the summer, compared with winter. This effect appears to outweigh any impact of reduced continentality given global average sea levels ca. 10 m higher during the late Miocene compared with modern (Miller et al., 2005). A likely return to similar ice coverage over the coming century (Sigmond et al., 2018) may drive a shift to more enhanced seasonal precipitation regimes similar to those we infer for the Tortonian.

~~5.5 Near-future Arctic climate and implications for permafrost thaw~~

~~Observational evidence suggests that annual and extreme precipitation is already increasing in permafrost regions and driving permafrost thaw in the Lena River basin . Whilst we are unable to quantify precipitation amount from our data, the enhanced precipitation volatility inferred for the Tortonian suggests annual and extreme precipitation will continue to increase given MAAT rises similar to those we infer for the Miocene and reduced sea-ice cover in the Arctic Ocean. This will likely further destabilise permafrost as extreme precipitation events increase soil moisture and, in turn, the latent heat of freezing .~~

~~Our speleothem records suggest a significantly warmer climate in the high Arctic during the Tortonian, with MAAT 18.9 - 23.4°C warmer than present. . Globally, Tortonian climate was similar to the end of the century projections under high emissions scenarios which predict between 2 - 5°C of warming . Global mean annual temperatures were some 4.5°C warmer than pre-industrial and atmospheric carbon dioxide concentrations up to 600 ppm .(Rae et al., 2021; Sosdian et al., 2018b; Super et al., 2018). Thus, our findings provide estimates for end-of-century Arctic temperature amplification and precipitation variability under high emissions scenarios. Our estimate is considerably higher than reconstructions for the middle Pliocene Warm Period (3.3 - 3.0 Ma) which suggested Arctic warming of 7.2°C given global mean temperatures 3.2°C above pre-industrial .~~Today, the Lena Delta region sits at the northern Eurasian terrestrial permafrost boundary and is underlain by deep, continuous permafrost . Arctic amplification of a magnitude similar to that reconstructed for the Tortonian would threaten the stability of permafrost across the entire Eurasian landmass, driving further carbon emissions in a positive feedback cycle. Evidence from ice wedge pseudomorphs suggests the onset of high latitude Northern Hemisphere permafrost formation occurred in the late Pliocene (~3 Ma) (Opel et al., 2024) and it is very likely that the Northern Hemisphere was permafrost free during the Tortonian (Vaks et al., in review).

675

~~Observational evidence suggests that annual and extreme precipitation is already increasing in permafrost regions and driving permafrost thaw in the Lena River basin . Whilst we are unable to quantify precipitation amount from our data, the enhanced precipitation volatility inferred for the Tortonian suggests annual and extreme precipitation will continue to increase given~~

680 ~~MAAT rises similar to those we infer for the Miocene and reduced sea-ice cover in the Arctic Ocean. This will likely further destabilise permafrost as extreme precipitation events increase soil moisture and, in turn, the latent heat of freezing .~~

Today, the Lena Delta region sits at the northern Eurasian terrestrial permafrost boundary and is underlain by deep, continuous permafrost of 400 – 600 m thickness . Arctic amplification of a magnitude similar to that reconstructed for the Tortonian would threaten the stability of permafrost across the entire Eurasian landmass, driving further carbon emissions in a positive feedback cycle. Evidence from ice-wedge pseudomorphs suggests the onset of high-latitude Northern Hemisphere permafrost formation occurred in the late Pliocene (~3 Ma) (Opel et al., 2024) and it is very likely that the Northern Hemisphere was permafrost-free during the Tortonian (Vaks et al., in review).

Using our new temperature reconstructions, we estimate total potential permafrost-derived carbon emissions given future warming similar to that reconstructed for the Tortonian and update the previous calculation from Vaks et al. (in review). These authors used the presence of speleothems alone to derive a more conservative (lower) Taba Bastaakh temperature limit of 5°C. Here we repeat their calculation using our upper and lower temperature estimates of ~6.6°C and 11.1°C, which amounts to an 18.9–23.4°C increase from the present day MAAT of 12.3°C. We calculate carbon emissions by overlaying vulnerable permafrost regions with a soil organic carbon (SOC) model (Palmtag et al., 2022) for the upper 3 metres of permafrost soil. Even considering a conservative permafrost boundary of MAAT = 0°C (often, colder temperatures down to MAAT = 8°C are required to sustain continuous permafrost), the warming by 18.9–23.4°C would thaw virtually all permafrost. With such levels of Arctic warming, 98-100 % of Northern Hemisphere permafrost area would be vulnerable to near-surface thaw (Fig. 7). This is slightly higher than recent middle Pliocene estimates from Guo et al. (2023), who found a 93 ± 3% decrease in permafrost extent based on a ca. 7.2°C warmer Arctic compared with pre-industrial temperatures. Based on Palmtag et al. (2022), which excludes the Tibetan Plateau region, we estimate at least 855 PgC is contained in permafrost that is vulnerable to thaw in the underlying 3 metres of soil. Of this, 5–15% (43–128 PgC) would likely be released to the atmosphere within decades (Schuur et al., 2022), while longer term emissions remain uncertain as new, expanding vegetation regimes stabilise and thawed regions either dry out or continue to sequester carbon as active wetlands.

Our estimate provides a first approximation of potential permafrost emissions by 2100 given global temperature rises similar to those projected by the end of century under high carbon emissions . We stress that our calculation assumes a constant 18.9 – 23.4°C temperature rise across all permafrost regions (equal to the reconstructed Tortonian temperature range at Taba Bastaakh) and undoubtedly simplifies spatial variability in warming. However, our findings suggest that permafrost thaw will contribute significantly to future carbon emissions, and we highlight the importance of including permafrost feedbacks in quantifying future emissions budgets.

6 Conclusions

720 We present the first speleothem derived temperature and precipitation seasonality records from Arctic Siberia during the Tortonian (11.63 – 7.246 Ma). Our findings offer insight into high latitude climate during a period when the global mean surface temperature was similar to that projected over the coming decades under high emission scenarios.

Apparent hydrologically driven element cycles suggest a more seasonal precipitation regime compared with the modern day,
725 likely driven by fluctuations in Arctic Sea ice extent. Given probable reductions in summer Arctic ice extent over the coming decades, a return to more volatile precipitation regimes seems likely, with increased summer precipitation driving permafrost thaw and impacting local infrastructure.

We use two independent methodologies to reconstruct the most northerly terrestrial Tortonian temperatures between 6.6°C
730 and 11.1~~8~~°C from high latitude central Siberia. These findings provide much needed estimates for future Arctic amplification, implying Arctic MAAT increases of 18.9−23.4°C above modern, given global mean temperature rises of ca. 4.5°C above pre-industrial. ~~are~~This is in good agreement with previous estimates from the region. ~~and support the consensus of a substantially~~ warmer late Miocene climate compared with modern day. Our findings confirm the long-established discrepancy between model simulations and proxy reconstructions, producing considerably higher estimates for Tortonian Arctic amplification than
735 models.

~~provide much needed estimates for future Arctic amplification, implying Arctic MAAT increases of 18.9−23.4°C above modern, given global mean temperature rises of ca. 4.5°C above pre-industrial—considerably higher than current estimates from climate models.~~

740

~~Amplified Arctic warming implied by our study would render the majority of Arctic and sub-Arctic surface permafrost free, resulting in an additional estimated 43-128 Pg of carbon emissions. This highlights the significant contribution of permafrost feedbacks to future emissions and the urgent need to incorporate them into future carbon budget calculations.~~

Author contributions

745 SU and SB conceptualised the study. AV, OS, AK, IA, and SB were responsible for sample collection. AV and GH provided U-Pb dating of samples. SU and SM performed clumped isotope analysis. FL and SU milled samples and performed stable isotope analysis. PS performed trace element analysis. YD performed fluid inclusion measurements. TB and AG contributed to interpretation of the dataset, with TB providing the comparison between Miocene and modern seasonal cycles (and production of figures 6, S8 and S9)~~, and AG responsible for calculating likely future emissions from permafrost (and~~

750 ~~production of figure 7)~~. SU oversaw writing of the manuscript and figure preparation, with significant input from FL, TO, SB, and AG. All authors contributed to the review and editing of the manuscript.

Competing Interests

The authors declare that they have no conflict of interest.

Data availability statement

755 All data will be included in this manuscript in the supporting information. Trace element, stable, and clumped isotope data ~~will be~~is archived in the ~~PANGAEA~~Zenodo database ~~pending acceptance of this manuscript~~(DOI 10.5281/zenodo.11476112).

Disclaimer

Any use of trade, firm, or product names is for descriptive purposes only and does not imply endorsement by the U.S. Government.

760 **Acknowledgements**

The authors would like to thank the Leverhulme Trust (RPG-2020-334), Natural Environment Research Council (NE/KE005057/1 awarded to A. Vaks), and Swiss National Science Foundation (grant P2EZP2_172213 awarded to F. Lechleitner) who funded this research. We thank Julian Murton at the University of Sussex, Arthur Oldeman at Utrecht University, and an anonymous reviewer for their constructive reviews and helpful comments, alongside Paul Dennis and

765 Norbert Marwan for acting as independent reviewers of the draft manuscript, and Alberto Reyes for his role as journal editor. We thank Birgit Schröder at GFZ Potsdam for providing the Plessen internal standard used in our stable isotope measurements. ~~and Paul Dennis and Norbert Marwan for acting as independent reviewers of the draft manuscript.~~ TB acknowledges fruitful discussions with Norbert Marwan.

References

770

Anderson, N. T., Kelson, J. R., Kele, S., Daëron, M., Bonifacie, M., Horita, J., Mackey, T. J., John, C. M., Kluge, T., Petschnig, P., Jost, A. B., Huntington, K. W., Bernasconi, S. M., and Bergmann, K. D.: A Unified Clumped Isotope Thermometer

Calibration (0.5–1,100°C) Using Carbonate-Based Standardization, Geophys Res Lett, 48, https://doi.org/10.1029/2020GL092069, 2021.

775 Baker, A., Hartmann, A., Duan, W., Hankin, S., Comas-Bru, L., Cuthbert, M. O., Treble, P. C., Banner, J., Genty, D., Baldini, L. M., Bartolomé, M., Moreno, A., Pérez-Mejías, C., and Werner, M.: Global analysis reveals climatic controls on the oxygen isotope composition of cave drip water, Nat Commun, 10, https://doi.org/10.1038/s41467-019-11027-w, 2019.

Baker, J. L., Lachniet, M. S., Chervyatsova, O., Asmerom, Y., and Polyak, V. J.: Holocene warming in western continental Eurasia driven by glacial retreat and greenhouse forcing, Nat Geosci, 10, 430–435, https://doi.org/10.1038/ngeo2953, 2017.

780 Bernasconi, S. M., Müller, I. A., Bergmann, K. D., and Breitenbach, S. F. M.: Reducing Uncertainties in Carbonate Clumped Isotope Analysis Through Consistent Carbonate-Based Standardization ~~Geochemistry~~ ,Geochemistry, ~~Geophysics~~ ,Geophysics, Geosystems, 2895–2914, https://doi.org/10.1029/2017GC007385, 2018.

Bernasconi, S. M., Daëron, M., Bergmann, K. D., Bonifacie, M., Meckler, A. N., Affek, H. P., Anderson, N., Bajnai, D., Barkan, E., Beverly, E., Blamart, D., Burgener, L., Calmels, D., Chaduteau, C., Clog, M., Davidheiser-Kroll, B., Davies, A.,
785 Dux, F., Eiler, J., Elliott, B., Fetrow, A. C., Fiebig, J., Goldberg, S., Hermoso, M., Huntington, K. W., Hyland, E., Ingalls, M., Jaggi, M., John, C. M., Jost, A. B., Katz, S., Kelson, J., Kluge, T., Kocken, I. J., Laskar, A., Leutert, T. J., Liang, D., Lucarelli, J., Mackey, T. J., Mangenot, X., Meinicke, N., Modestou, S. E., Müller, I. A., Murray, S., Neary, A., Packard, N., Passey, B. H., Pelletier, E., Petersen, S., Piasecki, A., Schauer, A., Snell, K. E., Swart, P. K., Tripati, A., Upadhyay, D., Vennemann, T., Winkelstern, I., Yarian, D., Yoshida, N., Zhang, N., and Ziegler, M.: InterCarb: A Community Effort to Improve
790 Interlaboratory Standardization of the Carbonate Clumped Isotope Thermometer Using Carbonate Standards, Geochemistry, Geophysics, Geosystems, 22, https://doi.org/10.1029/2020GC009588, 2021.

Berndt, D. J. and Clifford, J.: Using dynamic time warping to find patterns in time series, Proceedings of the 3rd international conference on knowledge discovery and data mining, 359–370, 1994.

~~Biskaborn, B. K., Smith, S. L., Noetzli, J., Matthes, H., Vieira, G., Streletskiy, D. A., Schoeneich, P., Romanovsky, V. E.,~~
795 ~~Lewkowicz, A. G., Abramov, A., Allard, M., Boike, J., Cable, W. L., Christiansen, H. H., Delaloye, R., Diekmann, B.,~~
~~Drozdov, D., Etzelmüller, B., Grosse, G., Guglielmin, M., Ingeman-Nielsen, T., Isaksen, K., Ishikawa, M., Johansson, M.,~~
~~Johannsson, H., Joo, A., Kaverin, D., Kholodov, A., Konstantinov, P., Kröger, T., Lambiel, C., Lanckman, J. P., Luo, D.,~~
~~Malkova, G., Meiklejohn, I., Moskalenko, N., Oliva, M., Phillips, M., Ramos, M., Sannel, A. B. K., Sergeev, D., Seybold, C.,~~
~~Skryabin, P., Vasiliev, A., Wu, Q., Yoshikawa, K., Zheleznyak, M., and Lantuit, H.: Permafrost is warming at a global scale,~~
800 ~~Nat Commun, 10, https://doi.org/10.1038/s41467-018-08240-4, 2019.~~

Boike, J., Kattenstroth, B., Abramova, K., Bornemann, N., Chetverova, A., Fedorova, I., Fröb, K., Grigoriev, M., Grüber, M., Kutzbach, L., Langer, M., Minke, M., Muster, S., Piel, K., Pfeiffer, E. M., Stoof, G., Westermann, S., Wischnewski, K., Wille, C., and Hubberten, H. W.: Baseline characteristics of climate, permafrost and land cover from a new permafrost observatory in the Lena River Delta, Siberia (1998-2011), Biogeosciences, 10, 2105–2128, https://doi.org/10.5194/bg-10-2105-2013,
805 2013.

Boike, J., Nitzbon, J., Anders, K., Grigoriev, M., Bolshiyanov, D., Langer, M., Lange, S., Bornemann, N., Morgenstern, A., Schreiber, P., Wille, C., Chadburn, S., Gouttevin, I., Burke, E., and Kutzbach, L.: A 16-year record (2002-2017) of permafrost, active-layer, and meteorological conditions at the Samoylov Island Arctic permafrost research site, Lena River delta, northern Siberia: An opportunity to validate remote-sensing data and land surface, snow, and permafrost models, Earth Syst Sci Data, 11, 261–299, https://doi.org/10.5194/essd-11-261-2019, 2019.

810

Bonne, J. L., Meyer, H., Behrens, M., Boike, J., Kipfstuhl, S., Rabe, B., Schmidt, T., Schönicke, L., Steen-Larsen, H. C., and Werner, M.: Moisture origin as a driver of temporal variabilities of the water vapour isotopic composition in the Lena River Delta, Siberia, Atmos Chem Phys, 20, 10493–10511, https://doi.org/10.5194/acp-20-10493-2020, 2020.

Borsato, A., Frisia, S., Fairchild, I. J., Somogyi, A., and Susini, J.: Trace element distribution in annual stalagmite laminae

815 mapped by micrometer-resolution X-ray fluorescence: Implications for incorporation of environmentally significant species, Geochim Cosmochim Acta, 71, 1494–1512, https://doi.org/10.1016/j.gca.2006.12.016, 2007.

Bradshaw, C. D., Lunt, D. J., Flecker, R., Salzmann, U., Pound, M. J., Haywood, A. M., and Eronen, J. T.: The relative roles of CO_2 and palaeogeography in determining late Miocene climate: Results from a terrestrial model-data comparison, Climate of the Past, 8, 1257–1285, https://doi.org/10.5194/cp-8-1257-2012, 2012.

820 Brand, W. A., Assonov, S. S., and Coplen, T. B.: Correction for the 17O interference in δ(13C) measurements when analyzing CO_2 with stable isotope mass spectrometry (IUPAC Technical Report), Pure and Applied Chemistry, 82, 1719–1733, https://doi.org/10.1351/PAC-REP-09-01-05, 2010.

Breitenbach, S. F. M. and Marwan, N.: Acquisition and analysis of greyscale data from stalagmites using ImageJ software, 69–78 pp., 2023.

825 Bruch, A. A., Utescher, T., and Mosbrugger, V.: Precipitation patterns in the Miocene of Central Europe and the development of continentality, Palaeogeogr Palaeoclimatol Palaeoecol, 304, 202–211, https://doi.org/10.1016/j.palaeo.2010.10.002, 2011.

Burls, N. J., Bradshaw, C. D., De Boer, A. M., Herold, N., Huber, M., Pound, M., Donnadieu, Y., Farnsworth, A., Frigola, A., Gasson, E., von der Heydt, A. S., Hutchinson, D. K., Knorr, G., Lawrence, K. T., Lear, C. H., Li, X., Lohmann, G., Lunt, D. J., Marzocchi, A., Prange, M., Riihimaki, C. A., Sarr, A. C., Siler, N., and Zhang, Z.: Simulating Miocene Warmth: Insights

830 From an Opportunistic Multi-Model Ensemble (MioMIP1), Paleoceanogr Paleoclimatol, 36, https://doi.org/10.1029/2020PA004054, 2021.

Chylek, P., Folland, C., Klett, J. D., Wang, M., Hengartner, N., Lesins, G., and Dubey, M. K.: Annual Mean Arctic Amplification 1970–2020: Observed and Simulated by CMIP6 Climate Models, Geophys Res Lett, 49, https://doi.org/10.1029/2022GL099371, 2022.

835 Coplen, T. B.: Calibration of the calcite–water oxygen-isotope geothermometer at Devils Hole, Nevada, a natural laboratory, Geochim Cosmochim Acta, 71, 3948–3957, https://doi.org/10.1016/j.gca.2007.05.028, 2007.

Craig, H.: Isotopic variations in meteoric waters, Science (1979), 133, 1702–1703, https://doi.org/10.1126/science.133.3465.1702, 1961.

Daëron, M.: Full Propagation of Analytical Uncertainties in Δ47 Measurements, Geochemistry, Geophysics, Geosystems, 22,

840 https://doi.org/10.1029/2020GC009592, 2021.

Daëron, M. and Gray, W. R.: Revisiting Oxygen-18 and Clumped Isotopes in Planktic and Benthic Foraminifera, Paleoceanogr Paleoclimatol, 38, https://doi.org/10.1029/2023PA004660, 2023.

Daëron, M., Blamart, D., Peral, M., and Affek, H. P.: Absolute isotopic abundance ratios and the accuracy of Δ47 measurements, Chem Geol, 442, 83–96, https://doi.org/10.1016/j.chemgeo.2016.08.014, 2016.

845 Dansgaard, W.: Stable isotopes in precipitation, ~~Tellus ,~~ Tellus, 16, 436–468, https://doi.org/10.3402/tellusa.v16i4.8993, 1964.

Dennis, K. J., Affek, H. P., Passey, B. H., Schrag, D. P., and Eiler, J. M.: Defining an absolute reference frame for 'clumped' isotope studies of CO_2, Geochim Cosmochim Acta, 75, 7117–7131, https://doi.org/10.1016/j.gca.2011.09.025, 2011.

Domínguez-Villar, D., Fairchild, I. J., Baker, A., Carrasco, R. M., and Pedraza, J.: Reconstruction of cave air temperature based on surface atmosphere temperature and vegetation changes: Implications for speleothem palaeoclimate records, Earth

850 Planet Sci Lett, 369–370, 158–168, https://doi.org/10.1016/j.epsl.2013.03.017, 2013.

Dublyansky, Y. V. and Spötl, C.: Hydrogen and oxygen isotopes of water from inclusions in minerals: Design of a new crushing system and on-line continous-flow isotope ratio mass spectrometric analysis, Rapid Communications in Mass Spectrometry, 23, 2605–2613, https://doi.org/10.1002/rcm.4155, 2009.

Eiler, J. M. and Schauble, E.: 18O13C16O in Earth's atmosphere, Geochim Cosmochim Acta, 68, 4767–4777,

855 https://doi.org/10.1016/j.gca.2004.05.035, 2004.

~~Farquharson, L. M., Romanovsky, V. E., Cable, W. L., Walker, D. A., Kokelj, S. V., and Nicolsky, D.: Climate Change Drives Widespread and Rapid Thermokarst Development in Very Cold Permafrost in the Canadian High Arctic, Geophys Res Lett, 46, 6681–6689, https://doi.org/10.1029/2019GL082187, 2019.~~

Fernandez, A., Müller, I. A., Rodríguez-Sanz, L., van Dijk, J., Looser, N., and Bernasconi, S. M.: A Reassessment of the

860 Precision of Carbonate Clumped Isotope Measurements: Implications for Calibrations and Paleoclimate Reconstructions, Geochemistry, Geophysics, Geosystems, 18, 4375–4386, https://doi.org/10.1002/2017GC007106, 2017.

Finestone, E. M., Breeze, P. S., Breitenbach, S. F. M., Drake, N., Bergmann, L., Maksudov, F., Muhammadiyev, A., Scott, P., Cai, Y., Khatsenovich, A. M., Rybin, E. P., Nehrke, G., Boivin, N., and Petraglia, M.: Paleolithic occupation of arid Central Asia in the Middle Pleistocene, PLoS One, 17, https://doi.org/10.1371/journal.pone.0273984, 2022.

865 Ford, J. D., McDowell, G., and Pearce, T.: The adaptation challenge in the Arctic, https://doi.org/10.1038/nclimate2723, 1 December 2015.

~~Froitzheim, N., Majka, J., and Zastrozhnov, D.: Methane release from carbonate rock formations in the Siberian permafrost area during and after the 2020 heat wave, Proc Natl Acad Sci U S A, 118, https://doi.org/10.1073/pnas.2107632118, 2021.~~

Gaskell, D. E., Huber, M., O'brien, C. L., Inglis, G. N., Acosta, R. P., Poulsen, C. J., and Hull, P. M.: The latitudinal

870 temperature gradient and its climate dependence as inferred from foraminiferal δ 18 O over the past 95 million years, 119, 2111332119, https://doi.org/10.1073/pnas, 2022.

Goldner, A., Herold, N., and Huber, M.: The challenge of simulating the warmth of the mid-Miocene climatic optimum in CESM1, Climate of the Past, 10, 523–536, https://doi.org/10.5194/cp-10-523-2014, 2014.

Hamma, J.: Drivers of permafrost degradation along the Inuvik to Tuktoyaktuk Highway (ITH), University of Potsdam, 2022.

875 Hartland, A., Fairchild, I. J., Lead, J. R., Borsato, A., Baker, A., Frisia, S., and Baalousha, M.: From soil to cave: Transport of trace metals by natural organic matter in karst dripwaters, Chem Geol, 304–305, 68–82, https://doi.org/10.1016/j.chemgeo.2012.01.032, 2012.

Harzhauser, M., Piller, W. E., Müllegger, S., Grunert, P., and Micheels, A.: Changing seasonality patterns in Central Europe from Miocene Climate Optimum to Miocene Climate Transition deduced from the Crassostrea isotope archive, Glob Planet 880 Change, 76, 77–84, https://doi.org/10.1016/j.gloplacha.2010.12.003, 2011.

Hao, Q., Wang, L., Oldfield, F., and Guo, Z.: Extra-long interglacial in Northern Hemisphere during MISs 15-13 arising from limited extent of Arctic ice sheets in glacial MIS 14, Sci Rep, 5, https://doi.org/10.1038/srep12103, 2015.

Herbert, T. D., Lawrence, K. T., Tzanova, A., Peterson, L. C., Caballero-Gill, R., and Kelly, C. S.: Late Miocene global cooling and the rise of modern ecosystems, Nat Geosci, 9, 843–847, https://doi.org/10.1038/ngeo2813, 2016.

885 Hofer, S., Lang, C., Amory, C., Kittel, C., Delhasse, A., Tedstone, A., and Fettweis, X.: Greater Greenland Ice Sheet contribution to global sea level rise in CMIP6, Nat Commun, 11, https://doi.org/10.1038/s41467-020-20011-8, 2020.

Huntington, K. W., Eiler, J. M., Affek, H. P., Guo, W., Bonifacie, M., Yeung, L. Y., Thiagarajan, N., Passey, B., Tripati, A., Daëron, M., and Came, R.: Methods and limitations of "clumped" CO_2 isotope ($\Delta 47$) analysis by gas-source isotope ratiomass spectrometry, Journal of Mass Spectrometry, 44, 1318–1329, https://doi.org/10.1002/jms.1614, 2009.

890 Izokh, N. and Yazikov, A.: Discovery of Early Carboniferous conodonts in Northern Kharaulakh Ranges (lower reaches of the Lena River, northeastern Siberia, Arctic Russia), Revue de Micropaleontologie, 60, 213–232, https://doi.org/10.1016/j.revmic.2017.03.001, 2017.

Jens Strauss, J., Matthias Fuchs, M., Gustaf Hugelius, G., Frederieke Miesner, F., Ingmar Nitze, I., Sophie Opfergelt, S., Edward Schuur, E., Claire Treat, C., Merritt Turetsky, M., Yuanhe Yang, Y., and Guido Grosse, G: Organic matter storage 895 and vulnerability in the permafrost domain, in: Reference Module in Earth Systems and Environmental Sciences, Elsevier, https://doi.org/https://doi.org/10.1016/B978-0-323-99931-1.00164-1, 2024.

John, C. M. and Bowen, D.: Community software for challenging isotope analysis: First applications of 'Easotope' to clumped isotopes, Rapid Communications in Mass Spectrometry, 30, 2285–2300, https://doi.org/10.1002/rcm.7720, 2016.

Johnson, K. R., Hu, C., Belshaw, N. S., and Henderson, G. M.: Seasonal trace-element and stable-isotope variations in a 900 Chinese speleothem: The potential for high-resolution paleomonsoon reconstruction, Earth Planet Sci Lett, 244, 394–407, https://doi.org/10.1016/j.epsl.2006.01.064, 2006.

Lachniet, M. S.: Climatic and environmental controls on speleothem oxygen-isotope values, Quat Sci Rev, 28, 412–432, https://doi.org/10.1016/j.quascirev.2008.10.021, 2009.

Lechleitner, F. A., Mason, A. J., Breitenbach, S. F. M., Vaks, A., Haghipour, N., and Henderson, G. M.: Permafrost-related
905   hiatuses in stalagmites: Evaluating the potential for reconstruction of carbon cycle dynamics, Quat Geochronol, 56, https://doi.org/10.1016/j.quageo.2019.101037, 2020.

Lewkowicz, A. G. and Way, R. G.: Extremes of summer climate trigger thousands of thermokarst landslides in a High Arctic environment, Nat Commun, 10, https://doi.org/10.1038/s41467-019-09314-7, 2019.

Liang, Y. C., Polvani, L. M., and Mitevski, I.: Arctic amplification, and its seasonal migration, over a wide range of abrupt
910   CO_2 forcing, NPJ Clim Atmos Sci, 5, https://doi.org/10.1038/s41612-022-00228-8, 2022.

Ma, N., Jiang, J. H., Hou, K., Lin, Y., Vu, T., Rosen, P. E., Gu, Y., and Fahy, K. A.: 21st Century Global and Regional Surface Temperature Projections, Earth and Space Science, 9, https://doi.org/10.1029/2022EA002662, 2022.

Mason, A. J., Vaks, A., Breitenbach, S. F. M., Hooker, J. N., and Henderson, G. M.: A simplified isotope dilution approach for the U-Pb dating of speleogenic and other low-232Th carbonates by multi-collector ICP-MS, Geochronology, 4, 33–54,
915   https://doi.org/10.5194/gchron-4-33-2022, 2022.

Masson-Delmotte, Valerie, Zhai, P., Pirani, A., Connors, S. L., Pean, C., Berger, S., Caud, N., Chen, Y., Goldfarb, L., Gomis, M., and others: Climate change 2021: the physical science basis, Contribution of working group I to the sixth assessment report of the intergovernmental panel on climate change, 2, 2021.

McKay, D. I. A., Staal, A., Abrams, J. F., Winkelmann, R., Sakschewski, B., Loriani, S., Fetzer, I., Cornell, S. E., Rockström,
920   J., and Lenton, T. M.: Exceeding 1.5°C global warming could trigger multiple climate tipping points, Science (1979), 377, https://doi.org/10.1126/science.abn7950, 2022.

Meinicke, N., Ho, S. L., Hannisdal, B., Nürnberg, D., Tripati, A., Schiebel, R., and Meckler, A. N.: A robust calibration of the clumped isotopes to temperature relationship for foraminifers, Geochim Cosmochim Acta, 270, 160–183, https://doi.org/10.1016/j.gca.2019.11.022, 2020.

925   Met Office Heathrow climatic averages 1991 – 2000, Retrieved 22 October 2024. Available at: https://www.metoffice.gov.uk/research/climate/maps-and-data/uk-climate-averages/gcpsvg3nc

Micheels, A., Bruch, A. A., Uhl, D., Utescher, T., and Mosbrugger, V.: A Late Miocene climate model simulation with ECHAM4/ML and its quantitative validation with terrestrial proxy data, Palaeogeogr Palaeoclimatol Palaeoecol, 253, 251–270, https://doi.org/10.1016/j.palaeo.2007.03.042, 2007.

930   Mikhaltsov et al.: Russian-German Cooperation: Expeditions to Siberia in 2017, edited by: Jens Strauss, Alfred-Wegener Institute, 90–107, 2018.

Miller, K. G., Kominz, M. A., Browning, J. V, Wright, J. D., Mountain, G. S., Katz, M. E., Sugarman, P. J., Cramer, B. S., Christie-Blick, N., and Pekar, S. F.: The Phanerozoic Record of Global Sea-Level Change, Science (1979), 310, 1293–1298, 2005.

935   Miller, K. G., Browning, J. V, Schmelz, W. J., Kopp, R. E., Mountain, G. S., and Wright, J. D.: Cenozoic sea-level and cryospheric evolution from deep-sea geochemical and continental margin records, 2020.

Milne, C. J., Kinniburgh, D. G., Van Riemsdijk, W. H., and Tipping, E.: Generic NICA - Donnan model parameters for metal-ion binding by humic substances, Environ Sci Technol, 37, 958–971, https://doi.org/10.1021/es0258879, 2003.

Moberg, A. Stockholm Historical Weather Observations — Monthly mean air temperatures since 1756. Dataset version 3. Bolin Centre Database. https://doi.org/10.17043/stockholm-historical-monthly-temperature-3, 2021.

Molnar, P.: Differences between soil and air temperatures: Implications for geological reconstructions of past climate, Geosphere, 18, 800–824, https://doi.org/10.1130/GES02448.1, 2022.

Moseley, G. E., Edwards, R. L., Lord, N. S., Spötl, C., and Cheng, H.: Speleothem record of mild and wet mid-Pleistocene climate in northeast Greenland, Sci. Adv, 2021.

Nazarenko, L. S., Tausnev, N., Russell, G. L., Rind, D., Miller, R. L., Schmidt, G. A., Bauer, S. E., Kelley, M., Ruedy, R., Ackerman, A. S., Aleinov, I., Bauer, M., Bleck, R., Canuto, V., Cesana, G., Cheng, Y., Clune, T. L., Cook, B. I., Cruz, C. A., Del Genio, A. D., Elsaesser, G. S., Faluvegi, G., Kiang, N. Y., Kim, D., Lacis, A. A., Leboissetier, A., LeGrande, A. N., Lo, K. K., Marshall, J., Matthews, E. E., McDermid, S., Mezuman, K., Murray, L. T., Oinas, V., Orbe, C., García-Pando, C. P., Perlwitz, J. P., Puma, M. J., Romanou, A., Shindell, D. T., Sun, S., Tsigaridis, K., Tselioudis, G., Weng, E., Wu, J., and Yao, M. S.: Future Climate Change Under SSP Emission Scenarios With GISS-E2.1, J Adv Model Earth Syst, 14, https://doi.org/10.1029/2021MS002871, 2022.

Nitzbon, J., Schneider von Deimling, T., Aliyeva, M., Chadburn, S. E., Grosse, G., Laboor, S., Lee, H., Lohmann, G., Steinert, N. J., Stuenzi, S. M., Werner, M., Westermann, S., & Langer, M. No respite from permafrost-thaw impacts in the absence of a global tipping point. *Nature Climate Change*, *14*(6), 573–585. https://doi.org/10.1038/s41558-024-02011-4. 2024

de Nooijer, W., Zhang, Q., Li, Q., Zhang, Q., Li, X., Zhang, Z., Guo, C., Nisancioglu, K. H., Haywood, A. M., Tindall, J. C., Hunter, S. J., Dowsett, H. J., Stepanek, C., Lohmann, G., Otto-Bliesner, B. L., Feng, R., Sohl, L. E., Chandler, M. A., Tan, N., Contoux, C., Ramstein, G., Baatsen, M. L. J., Von Der Heydt, A. S., Chandan, D., Peltier, W. R., Abe-Ouchi, A., Chan, W. Le, Kamae, Y., and Brierley, C. M.: Evaluation of Arctic warming in mid-Pliocene climate simulations, Climate of the Past, 16, 2325–2341, https://doi.org/10.5194/cp-16-2325-2020, 2020.

Opel, T., Bertran, P., Grosse, G., Jones, M., Luetscher, M., Schirrmeister, L., Stadelmaier, K. H., and Veremeeva, A.: Ancient permafrost and past permafrost in the Northern Hemisphere. In: Elias, S. (eds.) Encyclopedia of Quaternary Science, 3rd Edition. vol. 5, pp. 16-33. UK: Elsevier. dx.doi.org/10.1016/B978-0-323-99931-1.00258-0, Reference Module in Earth Systems and Environmental Sciences, Elsevier, https://doi.org/https://doi.org/10.1016/B978-0-323-99931-1.00258-0, 20254.

Orland, I. J., Burstyn, Y., Bar-Matthews, M., Kozdon, R., Ayalon, A., Matthews, A., and Valley, J. W.: Seasonal climate signals (1990-2008) in a modern Soreq Cave stalagmite as revealed by high-resolution geochemical analysis, Chem Geol, 363, 322–333, https://doi.org/10.1016/j.chemgeo.2013.11.011, 2014.

Oster, J. L., Ronay, E. R., Sharp, W. D., Breitenbach, S. F. M., and Furbish, D. J.: Controls on Speleothem Initial 234U/238U Ratios in a Monsoon Climate, Geochemistry, Geophysics, Geosystems, 24, https://doi.org/10.1029/2023GC010899, 2023.

Peel, M. C., Finlayson, B. L., and Mcmahon, T. A.: Hydrology and Earth System Sciences Updated world map of the Köppen-Geiger climate classification, Hydrol. Earth Syst. Sci, 1633–1644 pp., 2007.

Petersen, S. V., Winkelstern, I. Z., Lohmann, K. C., and Meyer, K. W.: The effects of Porapak(TM) trap temperature on d18O, d13C, and D47 values in preparing samples for clumped isotope analysis, Rapid Communications in Mass Spectrometry, 30, 1–10, https://doi.org/10.1002/rcm.7438, 2015.

Pflitsch, A. and Piasecki, J.: Detection of an airflow system in Niedzwiedzia (Bear) Cave, Kletno, Poland, Journal of Cave and Karst Studies, 65, 160–173, 2003.

Pionke, H. B., Gburek, W. J., Sharpley, A. N., and Zollweg, J. A.: Hydrological and chemical controls on phosphorus loss from catchments, in: Phosphorus Loss From Soil to Water, CAB International, Wallingford, 225–242, 1997.

Popova, S., Utescher, T., Gromyko, D., Bruch, A. A., and Mosbrugger, V.: Palaeoclimate evolution in Ssiberia and the Russian far east from the oligoceneOligocene to pliocenePliocene - evidence from fruit and seed floras, Turkish Journal of Earth Sciences, 21, 315–334, https://doi.org/10.3906/yer-1005-6, 2012.

Pound, M. J., Haywood, A. M., Salzmann, U., Riding, J. B., Lunt, D. J., and Hunter, S. J.: A Tortonian (Late Miocene, 11.61-7.25Ma) global vegetation reconstruction, Palaeogeogr Palaeoclimatol Palaeoecol, 300, 29–45, https://doi.org/10.1016/j.palaeo.2010.11.029, 2011.

Pound, M. J., Haywood, A. M., Salzmann, U., and Riding, J. B.: Global vegetation dynamics and latitudinal temperature gradients during the Mid to Late Miocene (15.97-5.33Ma), https://doi.org/10.1016/j.earscirev.2012.02.005, April 2012.

Rae, J. W. B., Zhang, Y. G., Liu, X., Foster, G. L., Stoll, H. M., and Whiteford, R. D. M.: Atmospheric CO 2 over the Past 66 Million Years from Marine Archives, The Annual Review of Earth and Planetary Sciences is online at earth.annualreviews.org, 49, 609–650, https://doi.org/10.1146/annurev-earth-082420, 2021.

Rantanen, M., Karpechko, A. Y., Lipponen, A., Nordling, K., Hyvärinen, O., Ruosteenoja, K., Vihma, T., and Laaksonen, A.: The Arctic has warmed nearly four times faster than the globe since 1979, Commun Earth Environ, 3, https://doi.org/10.1038/s43247-022-00498-3, 2022.

Rodrigues, T., Voelker, A. H. L., Grimalt, J. O., Abrantes, F., and Naughton, F.: Iberian Margin sea surface temperature during MIS 15 to 9 (580-300 ka): Glacial suborbital variability versus interglacial stability, Paleoceanography, 26, https://doi.org/10.1029/2010PA001927, 2011.

Runge, A., Nitze, I., and Grosse, G.: Remote sensing annual dynamics of rapid permafrost thaw disturbances with LandTrendr, Remote Sens Environ, 268, https://doi.org/10.1016/j.rse.2021.112752, 2022.

Schubert, B. A., Jahren, A. H., Davydov, S. P., and Warny, S.: The transitional climate of the late Miocene Arctic: Winter dominated precipitation with high seasonal variability, Geology, 45, 447–450, https://doi.org/10.1130/G38746.1, 2017.

Sherwin, C. M. and Baldini, J. U. L.: Cave air and hydrological controls on prior calcite precipitation and stalagmite growth rates: Implications for palaeoclimate reconstructions using speleothems, Geochim Cosmochim Acta, 75, 3915–3929, https://doi.org/10.1016/j.gca.2011.04.020, 2011.

Sigmond, M., Fyfe, J. C., and Swart, N. C.: Ice-free Arctic projections under the Paris Agreement, Nat Clim Chang, 8, 404–408, https://doi.org/10.1038/s41558-018-0124-y, 2018.

Sliwinski, J. T., Kost, O., Endres, L., Iglesias, M., Haghipour, N., González-Lemos, S., and Stoll, H. M.: Exploring soluble and colloidally transported trace elements in stalagmites: The strontium-yttrium connection, Geochim Cosmochim Acta, 343, 64–83, https://doi.org/10.1016/j.gca.2022.12.023, 2023.

Smith, D. M., Scaife, A. A., Eade, R., Athanasiadis, P., Bellucci, A., Bethke, I., Bilbao, R., Borchert, L. F., Caron, L. P., Counillon, F., Danabasoglu, G., Delworth, T., Doblas-Reyes, F. J., Dunstone, N. J., Estella-Perez, V., Flavoni, S., Hermanson, L., Keenlyside, N., Kharin, V., Kimoto, M., Merryfield, W. J., Mignot, J., Mochizuki, T., Modali, K., Monerie, P. A., Müller, W. A., Nicolí, D., Ortega, P., Pankatz, K., Pohlmann, H., Robson, J., Ruggieri, P., Sospedra-Alfonso, R., Swingedouw, D., Wang, Y., Wild, S., Yeager, S., Yang, X., and Zhang, L.: North Atlantic climate far more predictable than models imply, Nature, 583, 796–800, https://doi.org/10.1038/s41586-020-2525-0, 2020.

Sosdian, S. M., Greenop, R., Hain, M. P., Foster, G. L., Pearson, P. N., and Lear, C. H.: Constraining the evolution of Neogene ocean carbonate chemistry using the boron isotope pH proxy, Earth Planet Sci Lett, 498, 362–376, https://doi.org/10.1016/j.epsl.2018.06.017, 2018.

Spors, S.: Stable Water Isotope Characteristics of Recent Precipitation from Tiksi and Samoylov Island-Calibration of a Geoscientific Proxy for Northern Siberia: Bachelors Thesis, Institut für Erd- und Umweltwissenschaften, Universität Potsdam, Potsdam, 2018.

Spötl, C. and Vennemann, T. W.: Continuous-flow isotope ratio mass spectrometric analysis of carbonate minerals, https://doi.org/10.1002/rcm.1010, 2003.

Stein, R., Fahl, K., Schreck, M., Knorr, G., Niessen, F., Forwick, M., Gebhardt, C., Jensen, L., Kaminski, M., Kopf, A., Matthiessen, J., Jokat, W., and Lohmann, G.: Evidence for ice-free summers in the late Miocene central Arctic Ocean, Nat Commun, 7, https://doi.org/10.1038/ncomms11148, 2016.

Steinthorsdottir, M., Jardine, P. E., and Rember, W. C.: Near-Future pCO$_2$ During the Hot Miocene Climatic Optimum, Paleoceanogr Paleoclimatol, 36, https://doi.org/10.1029/2020PA003900, 2021a.

Steinthorsdottir, M., Coxall, H. K., de Boer, A. M., Huber, M., Barbolini, N., Bradshaw, C. D., Burls, N. J., Feakins, S. J., Gasson, E., Henderiks, J., Holbourn, A. E., Kiel, S., Kohn, M. J., Knorr, G., Kürschner, W. M., Lear, C. H., Liebrand, D., Lunt, D. J., Mörs, T., Pearson, P. N., Pound, M. J., Stoll, H., and Strömberg, C. A. E.: The Miocene: The Future of the Past, Paleoceanogr Paleoclimatol, 36, https://doi.org/10.1029/2020PA004037, 2021b.

Stoll, H. M., Müller, W., and Prieto, M.: I-STAL, a model for interpretation of Mg/Ca, Sr/Ca and Ba/Ca variations in speleothems and its forward and inverse application on seasonal to millennial scales, Geochemistry, Geophysics, Geosystems, 13, https://doi.org/10.1029/2012GC004183, 2012.

Super, J. R., Thomas, E., Pagani, M., Huber, M., O'Brien, C., and Hull, P. M.: North Atlantic temperature and pCO$_2$ coupling in the early-middle Miocene, Geology, 46, 519–522, https://doi.org/10.1130/G40228.1, 2018.

Taylor, P. C., Boeke, R. C., Boisvert, L. N., Feldl, N., Henry, M., Huang, Y., Langen, P. L., Liu, W., Pithan, F., Sejas, S. A., and Tan, I.: Process Drivers, Inter-Model Spread, and the Path Forward: A Review of Amplified Arctic Warming, https://doi.org/10.3389/feart.2021.758361, 9 February 2022.

Töchterle, P., Baldo, A., Murton, J. B., Schenk, F., Lawrence Edwards, R., Koltai, G., and Moseley, G. E.: Reconstructing Younger Dryas ground temperature and snow thickness from cave deposits, Climate of the Past, 20, 1521–1535, 1040 https://doi.org/10.5194/cp-20-1521-2024, 2024.

Tooth, A. F. and Fairchild, I. J.: Soil and karst aquifer hydrological controls on the geochemical evolution of speleothem-forming drip waters, Crag Cave, southwest Ireland, J Hydrol (Amst), 273, 2003.

Treble, P. C., Fairchild, I. J., Griffiths, A., Baker, A., Meredith, K. T., Wood, A., and McGuire, E.: Impacts of cave air ventilation and in-cave prior calcite precipitation on Golgotha Cave dripwater chemistry, southwest Australia, Quat Sci Rev, 1045 127, 61–72, https://doi.org/10.1016/j.quascirev.2015.06.001, 2015.

Tremaine, D. M. and Froelich, P. N.: Speleothem trace element signatures: A hydrologic geochemical study of modern cave dripwaters and farmed calcite, Geochim Cosmochim Acta, 121, 522–545, https://doi.org/10.1016/j.gca.2013.07.026, 2013.

Tremaine, D. M., Froelich, P. N., and Wang, Y.: Speleothem calcite farmed in situ: Modern calibration of δ18O and δ13C paleoclimate proxies in a continuously-monitored natural cave system, Geochim Cosmochim Acta, 75, 4929–4950, 1050 https://doi.org/10.1016/j.gca.2011.06.005, 2011.

Vaks, A., Mason, A. J., Breitenbach, S. F. M., Kononov, A. M., Osinzev, A. V., Rosensaft, M., Borshevsky, A., Gutareva, O. S., and Henderson, G. M.: Palaeoclimate evidence of vulnerable permafrost during times of low sea ice, Nature, 577, 221–225, https://doi.org/10.1038/s41586-019-1880-1, 2020.

Vaks, A., Mason, A., Breitenbach, S.F.M., Giesche, A., Osinzev, A., Yakshina., I., Kononov, A., Umbo, S., Lechleitner, F., 1055 Rosensaft, M. Borshevsky, A., and Henderson, G. M. Arctic speleothems reveal Late Miocene permafrost-free Northern Hemisphere, Nature Comms. 2024 (in review)

Vihma, T.: Effects of Arctic Sea Ice Decline on Weather and Climate: A Review, Surv Geophys, 35, 1175–1214, https://doi.org/10.1007/s10712-014-9284-0, 2014.

Vihma, T. (2014). Effects of Arctic Sea Ice Decline on Weather and Climate: A Review. *Surveys in Geophysics*, *35*(5), 1175–1060 1214. https://doi.org/10.1007/s10712-014-9284-0

Wassenburg, J. A., Riechelmann, S., Schröder-Ritzrau, A., Riechelmann, D. F. C., Richter, D. K., Immenhauser, A., Terente, M., Constantin, S., Hachenberg, A., Hansen, M., and Scholz, D.: Calcite Mg and Sr partition coefficients in cave environments: Implications for interpreting prior calcite precipitation in speleothems, Geochim Cosmochim Acta, 269, 581–596, https://doi.org/10.1016/j.gca.2019.11.011, 2020.

1065 Westerhold, T., Marwan, N., Drury, A. J., Liebrand, D., Agnini, C., Anagnostou, E., Barnet, J. S. K., Bohaty, S. M., De Vleeschouwer, D., Florindo, F., Frederichs, T., Hodell, D. A., Holbourn, A. E., Kroon, D., Lauretano, V., Littler, K., Lourens, L. J., Lyle, M., Pälike, H., Röhl, U., Tian, J., Wilkens, R. H., Wilson, P. A., and Zachos, J. C.: An astronomically dated record of Earth's climate and its predictability over the last 66 million years, Science (1979), 369, 1383–1388, https://doi.org/10.1126/SCIENCE.ABA6853, 2020.

1070 Wigley, T. M. L. and Brown, M. C.: The physics of caves: in Ford, T.D. & Cullingford, C.H.D (eds.), in: The Science of Speleology, Academic Press, London, 329–358, 1976.

Xie, A., Zhu, J., Kang, S., Qin, X., Xu, B., and Wang, Y.: Polar amplification comparison among Earth's three poles under different socioeconomic scenarios from CMIP6 surface air temperature, Sci Rep, 12, https://doi.org/10.1038/s41598-022-21060-3, 2022.

1075   York, D., Evensen, N. M., Martínez, M. L., and De Basabe Delgado, J.: Unified equations for the slope, intercept, and standard errors of the best straight line, Am J Phys, 72, 367–375, https://doi.org/10.1119/1.1632486, 2004.